

UNIVERSIDADE FEDERAL DE SÃO CARLOS
CENTRO DE CIÊNCIAS EXATAS E DE TECNOLOGIA
PROGRAMA DE PÓS-GRADUAÇÃO EM CIÊNCIA E
ENGENHARIA DE MATERIAIS

**EVALUATION OF Ti-6Al-4V FRICTION SURFACING COATINGS REINFORCED
WITH CARBIDES**

Carlos Alberto Belei Feliciano

São Carlos – SP

2017

UNIVERSIDADE FEDERAL DE SÃO CARLOS
CENTRO DE CIÊNCIAS EXATAS E DE TECNOLOGIA
PROGRAMA DE PÓS-GRADUAÇÃO EM CIÊNCIA E
ENGENHARIA DE MATERIAIS

**EVALUATION OF Ti-6Al-4V FRICTION SURFACING COATINGS REINFORCED
WITH CARBIDES**

Carlos Alberto Belei Feliciano

Dissertation presented to
Programa de Pós-Graduação em Ciência e
Engenharia de Materiais to obtain the
MASTER OF SCIENCE DEGREE IN
MATERIALS SCIENCE AND ENGINEERING

Supervisor: Dr. Nelson Guedes de Alcântara

Grant Agency: CNPq (Process no. 131389/2016-5)

São Carlos - SP

2017

RESUME

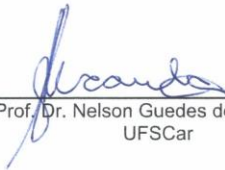
Engenheiro de Materiais pela Universidade Federal de São Carlos (2015).

**UNIVERSIDADE FEDERAL DE SÃO CARLOS**

Centro de Ciências Exatas e de Tecnologia
Programa de Pós-Graduação em Ciência e Engenharia de Materiais

Folha de Aprovação

Assinaturas dos membros da comissão examinadora que avaliou e aprovou a Defesa de Dissertação de Mestrado do candidato Carlos Alberto Belei Feliciano, realizada em 14/12/2017:



Prof. Dr. Nelson Guedes de Alcântara
UFSCar



Prof. Dr. Claudemiro Bolchini
UFSCar



Prof. Dr. Enrico José Giordano
CENIC

ACKNOWLEDGMENTS

I would like to thank my close relatives for all the love and support.

My professor Nelson for the important talks and for the opportunity to work and live abroad.

All Helmholtz-Zentrum Geesthacht employees.

CNPq for the financial support.

All my friends who stuck with me, from my hometown to Hamburg. You know who you are. Special thanks to my good friend Bruno (“Cebola”) without whom none of this would happen.

My supervisors Viktoria and Stefanie for the mentorship. This work would not be possible without them. And also for the fun times and friendship.

My parents for everything I have.

ABSTRACT

Friction surfacing is a thermo-mechanical process employed to deposit coatings in solid state resorting to friction between a rotating consumable rod and a substrate. The current work focuses on deposition of Ti-6Al-4V coatings reinforced with carbide particles (TiC, B₄C and SiC) on Ti-6Al-4V substrate. Particles were added using holes drilled into the rod tip. Different configurations of hole placements within the rod were correlated with process behavior, coating quality, deposition efficiency and particle distribution within the deposits. Configurations varied in number of holes and their distance to the rod's cross-sectional center. Holes placed near to the rod center increased axial forces during the plastification stage, whereas particles in holes far off the rod center were mainly expelled, not yielding as much effect on the process response. An increase in number of holes amplified the effects of the hole distance. The axial force during plastification stage affected both coating appearance and process efficiency. No full intermixing of coating material and particles during deposition occurred, thereby preventing a uniform distribution of particles throughout the coatings. Particles were mostly deposited along trails, which influenced the behavior of growing grains during recrystallization. B₄C and SiC particles underwent dissolution, whose degree was influenced by the rotational speed. Moreover, a refined α -Ti microstructure was reported, related to the development of shear bands independent of the particles' presence.

Keywords: Friction welding; Friction surfacing; Metal-matrix composites.

AVALIAÇÃO DA DEPOSIÇÃO POR FRICÇÃO DA LIGA Ti-6Al-4V COM REFORÇO DE CARBETOS

RESUMO

A deposição por fricção (FS) é um processo termomecânico utilizado na deposição em estado sólido de camadas através da fricção entre uma barra metálica, consumível, e um substrato. O presente trabalho foca na deposição da liga Ti-6Al-4V com reforço de carbeto (TiC, B₄C e SiC) em forma de partículas sobre um substrato da mesma liga. Partículas foram adicionadas utilizando furos feitos na extremidade da barra consumível. Diferentes configurações no que diz respeito ao posicionamento e à quantidade de furos na mesma barra foram relacionadas com o comportamento do processo, qualidade e eficiência das deposições e distribuição do reforço ao longo da seção transversal do depósito. Furos posicionados próximos do centro da seção transversal da barra acarretaram no aumento da força axial exercida pela máquina durante o estágio inicial de plastificação, enquanto furos mais distantes do centro foram em sua maioria expelidos, não tendo, assim, influência na resposta do processo. A força axial durante o estágio de plastificação afetou tanto a qualidade quanto a eficiência da deposição. O aumento no número de furos posicionados a mesma distância do centro da barra apenas amplificou tais efeitos. Não houve total mistura entre metal e reforço, o que preveniu uma distribuição uniforme de partículas ao longo do depósito. Partículas foram principalmente depositadas ao longo de faixas, o que influenciou de certa forma o crescimento dos grãos na recristalização durante o processo. Partículas de B₄C e SiC sofreram dissolução, cujo grau foi dependente da velocidade de rotação da barra consumível. Por fim, uma microestrutura refinada composta de α -Ti foi observada. Esta é associada à ocorrência de bandas de cisalhamento e não depende da presença de partículas.

Palavras-chave: Soldagem por fricção; Deposição por fricção; Compósitos de matriz metálica.

PUBLICATIONS

Published papers on international journals:

- **BELEI, C.**; FITSEVA, V.; DOS SANTOS, J.F.; ALCÂNTARA, N.G.; HANKE, S.
*TiC particle reinforced Ti-6Al-4V friction surfacing coatings. **Surface & Coatings Technology**, v. 329, pages 163-173, 2017.*

TABLE OF CONTENTS

FOLHA DE APROVAÇÃO.....	i
ACKNOWLEDGMENTS.....	iii
ABSTRACT.....	v
RESUMO.....	vii
PUBLICATIONS.....	ix
TABLE OF CONTENTS.....	xi
TABLES LIST.....	xiii
FIGURES LIST.....	xv
SYMBOLS AND ABBREVIATIONS.....	xix
1. INTRODUCTION AND JUSTIFICATION.....	1
2. OBJECTIVES.....	3
3. LITERATURE REVIEW.....	5
3.1. Titanium and its alloys.....	5
3.1.1. Titanium grade 5 (Ti-6Al-4V).....	6
3.2. Carbides.....	11
3.2.1. Group 4 carbides.....	11
3.2.2. Covalent carbides.....	12
3.3. Metal-matrix composites: strengthening mechanisms.....	13
3.4. Friction-based processes.....	15
3.4.1. Friction Surfacing.....	16
3.4.2. Manufacture of metal-matrix composites.....	20
4. MATERIALS AND METHODS.....	23
4.1. Materials.....	23
4.2. Friction Surfacing process.....	24
4.2.1. Machine features.....	24
4.2.2. Process parameters.....	25
4.3. Hole configurations.....	26
4.4. Temperature measurements.....	28
4.5. Evaluation of coating quality by visual analysis.....	28
4.6. Metallographic sample preparation.....	28
4.7. Hardness measurements.....	29

5.	RESULTS AND DISCUSSION	31
5.1.	Influence of hole configuration on coating appearance.....	31
5.2.	Friction surfacing process response	32
5.3.	Particle distribution within the coatings	37
5.4.	Microstructure evolution.....	42
5.4.1.	The influence of particles on dynamic recrystallization and its effect on coating hardness	49
5.4.2.	Particle behavior: dissolution and fracture	55
6.	GENERAL DISCUSSION	71
7.	CONCLUSIONS	73
8.	SUGGESTIONS FOR FUTURE RESEARCH.....	75
9.	REFERENCES	77

TABLES LIST

Table 4.1 - Chemical composition of the base material consumable rod and plate (wt. %)	23
Table 5.1 - Results of EDS analysis performed on the highlighted area indicated on Figure 5.22.	57
Table 5.2 - Results from EDS measurements on spots (1) and (2), indicated on Figure 5.26.	63

FIGURES LIST

Figure 3.1 - Possible phase diagram configurations, depending upon the alloying element [17].	5
Figure 3.2 - Lamellar structure on Ti-6Al-4V [17].	7
Figure 3.3 - Widmanstätten structure on Ti-6Al-4V [21].	7
Figure 3.4 - Martensitic structure on Ti-6Al-4V [22].	8
Figure 3.5 – Schematics of a generic thermomechanical route deployed to obtain a bimodal microstructure on the Ti-6Al-4V alloy. Adapted from [17].	9
Figure 3.6 – Bimodal microstructure on Ti-6Al-4V [24].	9
Figure 3.7 – Fully equiaxed microstructure on Tu-6Al-4V [26].	10
Figure 3.8 - Relationship between hardness and temperature for group 4, 5 and 6 carbides [31].	12
Figure 3.9 – Relationship between particle radius and yield strength of a given material. The optimal strength is achieved at \check{R} , the point where the curve for cutting ($\sim R^{1/2}$) and bypassing ($\sim 1/R$) meet [39].	14
Figure 3.10 – Friction Surfacing process applying several successive layers of aluminum [55].	17
Figure 3.11 – Schematic depiction of the friction surfacing process showing different process stages acc. to [16].	18
Figure 3.12 – Visual representation of the material flow during the FS. Adapted from [66].	19
Figure 4.1 - Size distribution of TiC particles.	24
Figure 4.2 - Friction surfacing machine. 1) Spindle; 2) consumable rod; 3) moving table; 4) substrate (Helmholtz-Zentrum Geesthacht).	25
Figure 4.3 – A schematic of the reinforcement of Ti-6Al-4V rod (longitudinal section) with TiC particles.	27
Figure 4.4 - Experimental design deployed to evaluate the process feasibility. Inside each hole, TiC particles were inserted. Each condition was labeled with a code, which is displayed next to the drawings.	27
Figure 4.5 - A schematic of the thermocouple placement used for temperature measurements during the deposition process.	28

Figure 4.6 – Sketch of a generic coating divided in twelve blocks (labeled with roman numerals) according to the indicated dimensions.....	30
Figure 5.1 – Applied hole configurations and top view images of corresponding depositions. Configuration 3-A yielded an abnormally thin layer, comprised basically of oxides.	31
Figure 5.2 - Deposition efficiency calculated for the presented experiments. ...	32
Figure 5.3 - Axial force diagrams for configurations 3-A, 3-B, 3-C and without particles. The vertical dashed lines indicate the transition between initial plasticizing and deposition stage for each condition after 0.8 mm rod shortening	34
Figure 5.4 - Axial force vs. shortening of the rod (rod consumption) for 1, 2 and 3 holes at 2 mm (upper image) and at 8 mm (lower image) distance to the cross section center. Data from a deposition without particles is plotted in grey. The vertical dashed lines indicate the transition between plasticizing and deposition stage.....	35
Figure 5.5 – Red dashed line represents the approximate transition from the deposition with high, unstable axial forces to the deposition with stabilized 2 kN. Black arrows indicate the present of cracks on the smoother portion of the coating.....	36
Figure 5.6 – Polished cross-sections of 2-A, 2-B and 2-C configurations. A large agglomerate of particles is present at the middle section of the 2-A coating, whereas particles are distributed sparsely near the surface and at the edges of 2-B coating. No particles are observed in 2-C coating.....	39
Figure 5.7 – Clusters of particles found within the flash formed around the rod tip during experiment with 1-C configuration.	40
Figure 5.8– Cross-sections of 1-B and 3-B configurations extracted from the middle section of each coating	41
Figure 5.9 - Cross-sections extracted from the beginning of the coatings generated by 2-A configuration.....	42
Figure 5.10 – Typical temperature evolution during deposition (configuration 1-B).....	43

Figure 5.11 – (a) SEM (backscatter electron) images of the coating microstructure. The Ti-6Al-4V matrix displays Widmanstätten or martensitic alpha lamellae. (b) Regions containing small equiaxed grains (mostly between 1 and 2 μm).....	44
Figure 5.12 - Regions containing small equiaxed grains (mostly between 1 and 2 μm).....	45
Figure 5.13 – EBSD image revealing fine equiaxed alpha grains surrounded by large grains. High-angle (black) and low-angle boundaries (white) are highlighted (a). A hybrid image of the inverse pole Figureure and the image quality is presented in (b).	45
Figure 5.14 - Sequence of voids among equiaxed alpha grains.....	47
Figure 5.15 - OM image of an etched specimen where a trail of equiaxed grains can be observed slightly protruding over the matrix surface. Surrounded by that region is a pore with diameter of 34 μm	48
Figure 5.16 – Microstructure of a coating reinforced with particles (configuration 1-A). A trail of fine recrystallized α grains and a trail of deposited TiC particles can be observed in between which alpha lamellae are seen.	49
Figure 5.17 – OM photos showing examples of deposited particles embedded on the matrix (configuration 2-B). Yellow arrows indicate particles found at grain boundaries.	50
Figure 5.18 – Microstructure of the coating (configuration 1-A) shows TiC particles mainly deposited along trails delimited by white dashed lines.	52
Figure 5.19 – Above, cross-sections of 2-A, 2-B and 2-C configurations and their relative hardness for each block, in comparison to regular, non-reinforced coatings. Darker areas indicate the presence of particles. Below, the standard deviation for each of twelve blocks from measurements on the control group .	52
Figure 5.20 - OM photo of an area of very high particle density where pores can be observed. Configuration 2-B.....	54
Figure 5.21 - Distribution of hardness values from inner cross-sectional areas of samples extracted from two different configurations: 2-A (particle-rich) and 1-C (particle-free). In order to factor out oxygen absorption by outer cross-sectional areas, only the inner regions of the coatings were evaluated.	55

Figure 5.22 – B ₄ C particle embedded in Ti matrix by FS (rotational speed of 3000 min ⁻¹). EDS analysis was performed on the area highlighted by the red circle.	57
Figure 5.23 - Possible reactions involving boron, titanium and carbon, according to their Gibbs free energy of formation.	59
Figure 5.24 – Red dot represents the approximate composition of the spot measured by Figure 5.22, projected on a B-C-Ti ternary phase diagram. Adapted from [105].	60
Figure 5.25 - TiB whiskers appearing as a result of degradation of B ₄ C particles on process runs deposited with rotational speed of 3000 min ⁻¹	61
Figure 5.26 - Trail of precipitates delimited by red dashed lines (6000 min ⁻¹). EDS analysis performed on the precipitate-rich strip (1) and on a precipitate free surrounding region.	62
Figure 5.27 - Precipitate-rich region, where TiB whiskers are indicated by black arrows. Rotational speed of 6000 min ⁻¹	63
Figure 5.28 - SiC particle partially dissolved. Rotational speed of 6000 min ⁻¹ . .	65
Figure 5.29 - Particle size distribution for deposited TiC particles (a) and TiC particles before the process (b), according to measurements performed on OM and SEM images	66
Figure 5.30 – Small TiC particles along shear flow paths (delimited by red dashed lines). Larger particles within those paths elongated in a direction showed by yellow arrows.	67
Figure 5.31 – OM image of small SiC particles deposited in parallel to the yellow arrows within a shear flow path delimited by the red dashed lines. No important effects of particle dissolution were observed, as the rotational speed (3000 min ⁻¹) was not sufficient to degrade the reinforcement.	68
Figure 5.32 - Crack observed on a coating obtained from experiment with SiC particles. The borehole drilled at the rod center in this case contributed to poor mixture of reinforcement. Rotational speed of 6000 min ⁻¹	69

SYMBOLS AND ABBREVIATIONS

AS	Advancing Side
ASTM	American Standard for Testing of Materials
B ₄ C	Boron Carbide
EBSD	Electron Backscatter Diffraction
EDS	Energy-Dispersive Spectroscopy
HV	Vickers Hardness
MMC	Metal-Matrix Composite
FS	Friction Surfacing
FSSW	Friction Stir Spot Welding
FSW	Friction Stir Welding
OM	Optical Microscope
RS	Retreating Side
SEM	Scanning Electron Microscope
SiC	Silicon Carbide
T _β	Beta Transition Temperature
TiC	Titanium Carbide

1. INTRODUCTION AND JUSTIFICATION

Aerospace and automobile industries are continuously searching for alternative materials and processes in their efforts to decrease weight in order to reduce the fuel consumption and save natural resources. As weight reduction comes normally at the expense of the mechanical properties, which are important for structural components, the development of materials with high strength-to-density ratio has been extensively stimulated in the last decades. The deployment of aluminum and titanium alloys in several structural applications follows this trend [1], as well as the evolution of composite technologies, which are essential for the modern industry [2,3].

The desired mechanical properties of lightweight metal alloys can be further improved not only by work hardening or heat treatments, but also by reinforcing them e.g. through addition of hard particles. Such metal matrix composites (MMC) can be used in applications where specific combinations of thermal, chemical and especially mechanical properties are required. There are a vast number of manufacture methods able to reliably produce MMC's. Among those, friction-based methods have been proving worth of value in the composites manufacture [4–7], especially when one takes into account the complete absence of melting on this group of processes, along with all the advantages that a melting-free method may offer.

Friction Surfacing (FS) is a friction-based method, deployed on the production of coatings for applications where generally the improvement of surface properties such as hardness, wear and corrosion resistance in comparison to the bulk is needed. Similarly to other friction-based methods, the feasibility of generating metal-matrix composites coatings by FS has been shown [8–12], whereby a sensible increase in hardness and wear resistance in comparison to reinforcement-free FS coatings can be achieved. Those features are especially important for titanium alloys, which inherently exhibit a low wear resistance due to their high chemical activity and adhesion to other surfaces [13–

15]. Such a deficiency may be potentially overcome by the addition of hard particles.

The effect of the particles on process characteristics, their distribution within the coating material and their influence on the microstructure evolution is to date still unclear, especially for titanium alloys, whose FS depositions without reinforcement particles are already highly sensitive to even subtle changes on process parameters [16]. In such a still underdeveloped scenario, it would be therefore pointless to proceed with mechanical properties testing and studies of feasibility of industrial implementation alike.

Prior to any other kind of investigation, one must be able to produce high quality reinforced coatings, being “high quality” defined here as having good structural uniformity and high concentration of homogeneously dispersed particles with as low reinforcement loss as possible.

Thus, the purpose behind this study is to provide a general knowledge baseline on the friction surfacing of titanium alloys reinforced with particles. This basic understanding will serve as a mainstay for future studies aiming to locally improve surface properties by adding MMC layers to a given component.

2. OBJECTIVES

The main objective of this study is to determine the feasibility of the friction surfacing process applied to deposit Ti-6Al-4V carbide-reinforced coatings on substrates from the same alloy, concerning the technical aspects of the process.

Secondary objectives are: (i) to relate microstructural features of the reinforced coatings to their hardness and (ii) to observe particle behavior during the process and its effects on coatings' characteristics.

3. LITERATURE REVIEW

3.1. Titanium and its alloys

Titanium is a silver-colored transition metal, known by its outstanding specific strength, low thermic and electric conductivity and a relatively high melting point (up to 1670°C [17]), in comparison to aluminum, its main competitor in a number of applications.

Similarly to iron and other metals, titanium undergoes an allotropic transformation upon heating. This phenomenon changes its crystal structure from hexagonal close-packed (referred to as α -Ti) to body-centered cubic (β -Ti). The temperature at which this transformation occurs (T_β) depends upon the alloy composition (Figure 3.1 [17]): titanium grade 1 has a T_β of 890°C; alloys where β phase is predominant have T_β ranging from 700 °C and 900°C; $\alpha+\beta$ alloys reach T_β generally from 950°C to 1100°C [17]. Both α and β phases can coexist at room temperature, also depending upon alloy composition. Normally, titanium alloys are classified in three different classes, according to their composition at equilibrium: α , β and $\alpha+\beta$ alloys.

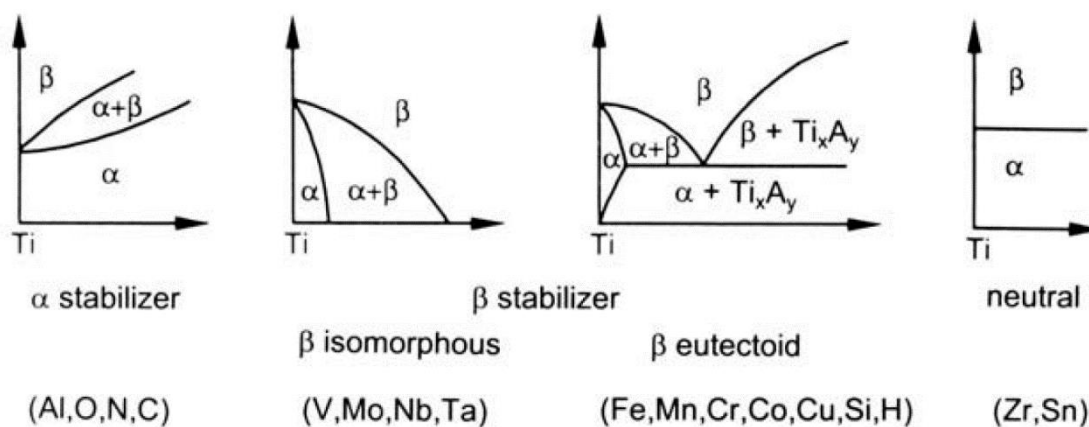


Figure 3.1 - Possible phase diagram configurations, depending upon the alloying element [17].

Titanium is highly reactive with oxygen. When exposed to an oxygen-rich atmosphere, this metal is converted to TiO_2 [17] and TiO (unstable, rapidly oxidized to TiO_2 [18]), constituting a layer frequently called oxide scale [18]. At room temperature, the oxide scale is a compact layer, which acts as a protective coat against other exterior gases. However, at high temperatures, such a layer becomes porous [18], increasing oxygen diffusion into the scale and ultimately reaching the base material. This eventually makes the oxide scale expand inwards at expense of the base material, as the oxidation goes on. Moreover, an oxygen-rich layer beneath the scale is formed simultaneously with the oxidation itself [17,19]. This interphase is referred to as α -case [17,20], since it is constituted by oxygen-stabilized α phase. Since the α -case is hard and less ductile [20], it may induce crack formation on the surface under mechanical loading [17]. Therefore, the use of an inert atmosphere during processing is essential for titanium alloys. Furthermore, this oxidation behavior renders the titanium useless on any situation taking place above 550°C , point beyond which oxygen diffusion into oxide scale drastically increases [17].

3.1.1. Titanium grade 5 (Ti-6Al-4V)

Created in 1954 [17], the titanium grade 5, also known as Ti-6Al-4V, is the most utilized titanium alloy worldwide. It contains aluminum ranging between 5.5 and 6.75%, and vanadium between 3.5 and 4.5% (according to ASTM B348-13). The composition in equilibrium is composed by α phase scattered uniformly in the β phase, which places the Ti-6Al-4V alloy under the " $\alpha+\beta$ alloys" category. The addition of V makes the β phase stable at room temperature and present in a volumetric fraction of approximately 15%.

Upon slow, controlled cooling of this alloy from the β field (T_β at 995°C [17]), α phase nucleates at beta grain boundaries, forming a continuous alpha layer surrounding beta grains. Next, alpha laths start to grow (individually parallel one to another and with the same Burgers relationship) from the beta grain boundaries inwards, until such laths make contact with each other. Such a structure is called lamellar, as evidenced by Figure 3.2 [17].

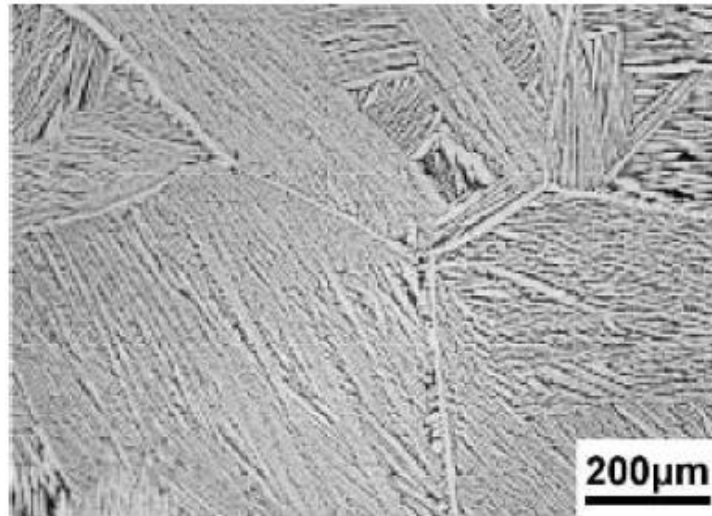


Figure 3.2 - Lamellar structure on Ti-6Al-4V [17].

As the cooling rate rises, alpha laths thin out. In this case, there is room for lath growth from the interface created between beta grain and alpha laths. In order to reduce elastic strain, such “secondary” laths grow perpendicularly to “primary” laths, which creates what is called “Widmanstätten structure” or “basket weave” (due to the similarities with the way handcrafted baskets are woven), Figure 3.3 [21]. Refined lamellae tend to result in higher yield stress, ductility and high-cycle fatigue resistance in comparison to coarse lamellae [17].

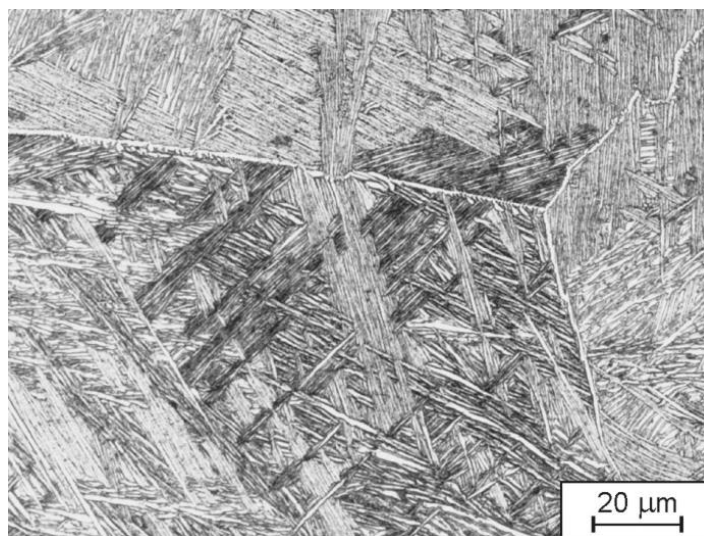


Figure 3.3 - Widmanstätten structure on Ti-6Al-4V [21].

For cooling rates above 1000°C/min, Widmanstätten structure ceases formation, giving rise to martensitic structure (Figure 3.4 [22]), which can be either α' (hexagonal) or α'' (orthorhombic) [17,23]. The main difference between the martensitic structure and the ones originated from mild cooling is that the martensite (i) shows needles dispersed all over the beta grain (with different Burgers relationships) and (ii) does not grow from the beta grain boundaries (which is the case for the aforementioned structures, originated from nucleation and growth).

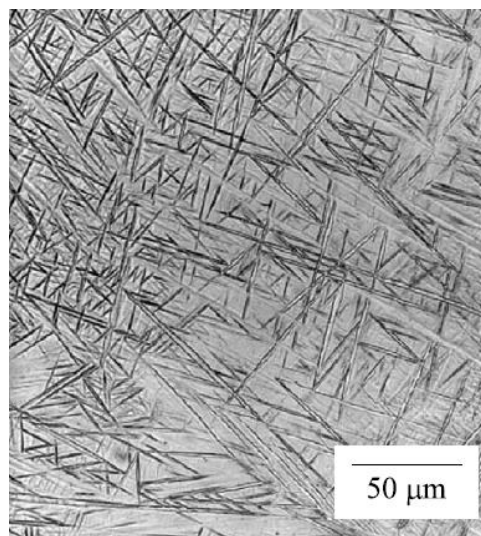


Figure 3.4 - Martensitic structure on Ti-6Al-4V [22].

Different thermomechanical routes (Figure 3.5 [17]) can modify the alloy's microstructure, turning it into bimodal instead of lamellar, as described previously. Generally, the homogenized material is deformed in the $\alpha+\beta$ field (Figure 3.5-II), which stores enough strain energy in both phases to trigger recrystallization, which is then induced by a third step, also below T_β (Figure 3.5-III).

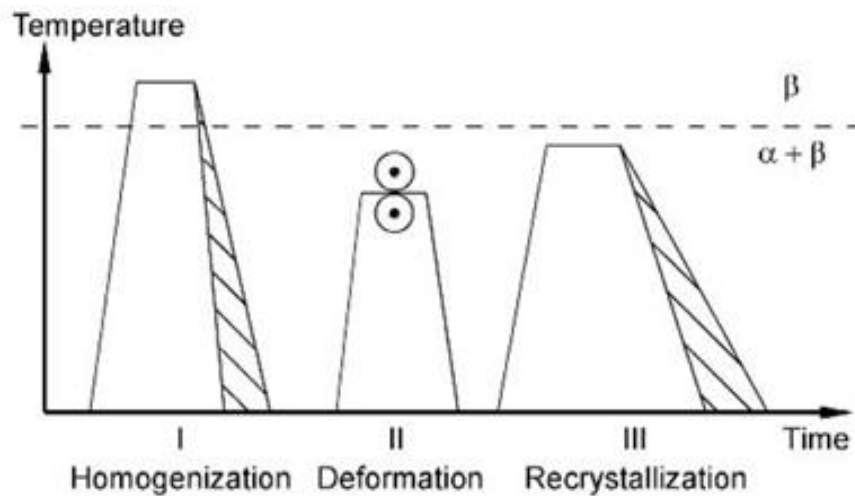


Figure 3.5 – Schematics of a generic thermomechanical route deployed to obtain a bimodal microstructure on the Ti-6Al-4V alloy. Adapted from [17].

During material recrystallization (Figure 3.5-III), alpha lamellae recrystallize, while beta grains grow along alpha/alpha grain boundaries, separating alpha grains to a distance approximately equal to the size of the beta grain. As a result, primary alpha grains are found at triple junctions. The rest of the microstructure is comprised by alpha laths grown from beta grain boundaries (Widmanstätten) as shown in Figure 3.6. Such a microstructure is named bimodal [17].

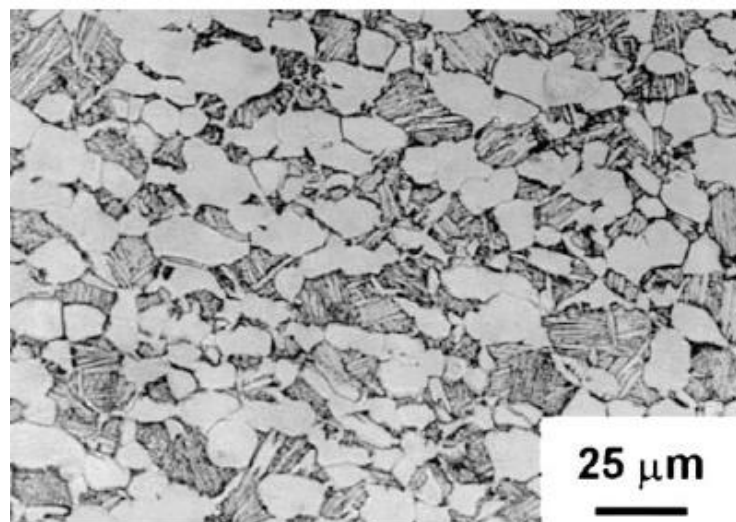


Figure 3.6 – Bimodal microstructure on Ti-6Al-4V [24]

With sufficiently low cooling rates from the recrystallization stage, alpha laths do not grow, which means that the entire alpha volumetric fraction would be represented by equiaxed alpha grains. Beta phase now is found at triple junctions between alpha grains (Figure 3.7), which constitutes a fully equiaxed microstructure [17]. Another parameter responsible for the occurrence of such a microstructure instead of the bimodal one is the temperature during the recrystallization stage. While a bimodal microstructure requires temperatures approximately as high as 970 °C, a fully equiaxed microstructure can be obtained at 800 °C [25].

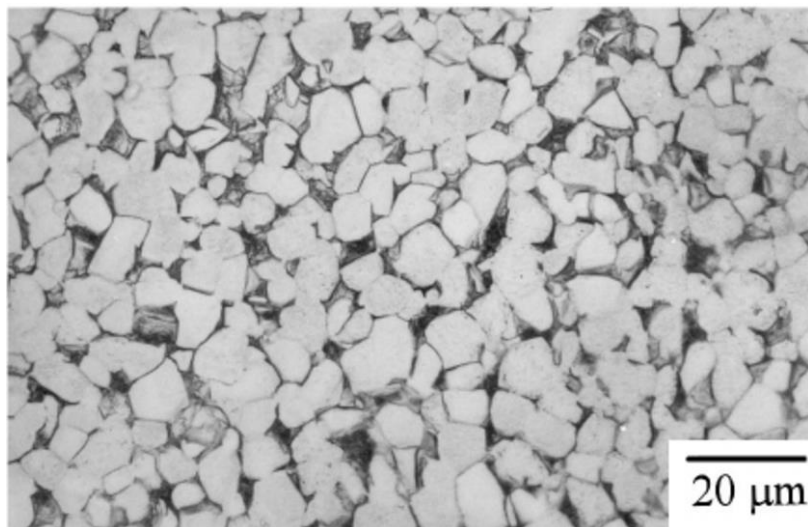


Figure 3.7 – Fully equiaxed microstructure on Ti-6Al-4V [26].

From the mechanical properties standpoint, it is known that the bimodal microstructure normally offers higher yield strength and ductility in comparison to the equiaxed one. However, the latter usually presents higher fatigue resistance than the former [17].

Since the Ti-6Al-4V alloy presents good mechanical strength and corrosion resistance coupled with its lightweight, this alloy can be deployed on a large number of applications, which range from structural components in airplanes to inner-body parts for humans and animals [27,28].

3.2. Carbides

Carbides are inorganic compounds formed by carbon and another element, which may be a metal or not. From the material science standpoint, carbides are classified as ceramic materials, usually with very high melting point and hardness. By comparison, while commercially-pure titanium has a hardness of approximately 55 HV, titanium carbide has 3200 HV; while the cp-Ti melts at 1640°C, the titanium carbide has a melting point clocking in at around 3000°C [29,30]. Thus, carbides are frequently used as reinforcement on metal-matrix composites, since such an addition enhances gains in properties such as hardness, wear resistance, creep resistance, and so forth.

3.2.1. Group 4 carbides

Carbides from the group 4 (titanium, zirconium, hafnium) are interstitial, as other carbides from groups 5 and 6. Their crystalline structure is the face-centered cubic (fcc), with carbon atoms, too large to fit into tetrahedral sites, occupying all the octahedral ones [30]. In this atomic arrangement, metal-to-metal bonds on those compounds are considered weak, whereas the carbon-to-metal bonds are strong [30]. The strength of those carbon-to-metal bonds prevents plastic deformation and makes those materials brittle, as normally occurs with other ceramics. However, those materials experience a brittle-ductile transition, which may occur at roughly 800°C, depending on factors such as grain size, composition and impurity content [31]. Another notable mechanical characteristic of those carbides is the drastic decrease in hardness with increasing temperature (Figure 3.8 [31]).

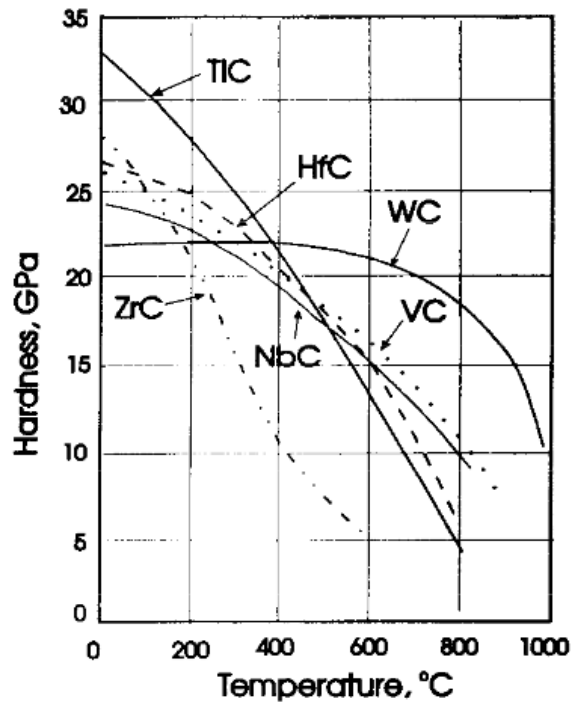


Figure 3.8 - Relationship between hardness and temperature for group 4, 5 and 6 carbides [31].

3.2.2. Covalent carbides

Covalent carbides comprise compounds from groups 13 and 14, most notably boron and silicon. As implied by their classification name, bonds on those materials are essentially covalent, although retaining a slight ionicity. Nevertheless, on those compounds covalent bonds are almost seven times as strong as the ionic ones [32]. On silicon carbide, each atom is surrounded by four atoms of the other element, with each atom having a coordination number of four [32]. On boron carbide, the shape of the unit cell is an icosahedron comprised of twelve boron atoms; those icosahedra have their centers at rhombohedron corners to form a boron carbide crystal. At the body diagonal of the rhombohedron is a three-atom chain (two carbon atoms surrounding one centralized boron one), forming a 15-atom unit cell [32]. Those materials are extremely hard. Boron carbide, for instance, comes after only diamond and cubic boron nitride on the list of hardest known materials, being able to maintain such a characteristic at temperatures as high as 1800°C [33]. Like

interstitial carbides, covalent carbides also show ductile-to-brittle transformation. In silicon carbide, for example, the temperature at which this transformation occurs hovers around 1100°C, depending on the stress state and strain rate [34]. Both silicon and boron carbide are basically inert at room temperature [32].

3.3. Metal-matrix composites: strengthening mechanisms

Metal-matrix composites (MMC's) are a class of materials comprising metallic alloys, wherein a foreign material is embedded. The embedded material (usually called reinforcement) may be ceramic or another metal and is usually shaped as particles. The interaction between the matrix and its reinforcements can originate several metallurgical phenomena, which are also influenced by the method utilized to assemble the material. Such phenomena are the main responsible for enhancing mechanical strength of the material. Some of the main strengthening mechanisms are namely:

Dislocation generation upon cooling: the difference between the thermal expansion coefficient of both matrix and reinforcement lead to a more intense matrix shrinkage in comparison to the reinforcement one. This induces the matrix to create dislocations in order to accommodate the reinforcement [35].

Reinforcement particles act hindering dislocation movement during deformation: as dislocations reach a reinforcement particle, they can either cut through or bypass the particle. Here, the initial size of particles is an important parameter, as it defines the behavior of dislocation movement when reaching such obstacles. Small, coherent particles (usually smaller than 1 μm [36]) are cut through by dislocation movement upon the deformation (phenomenon usually referred to as *Friedel cutting*) [37–39]. On the other hand, large particles are wrapped when reached by a moving dislocation, until the dislocation detaches from the obstacle and a loop is left around it (known as *Orowan bowing* or *bypassing*) [37,39–41]. The optimal mechanical strength, given by the particle presence in the metal matrix, occurs when the particle size is too large for the cut-through mechanism, but yet too small for the bypassing one (Figure 3.9).

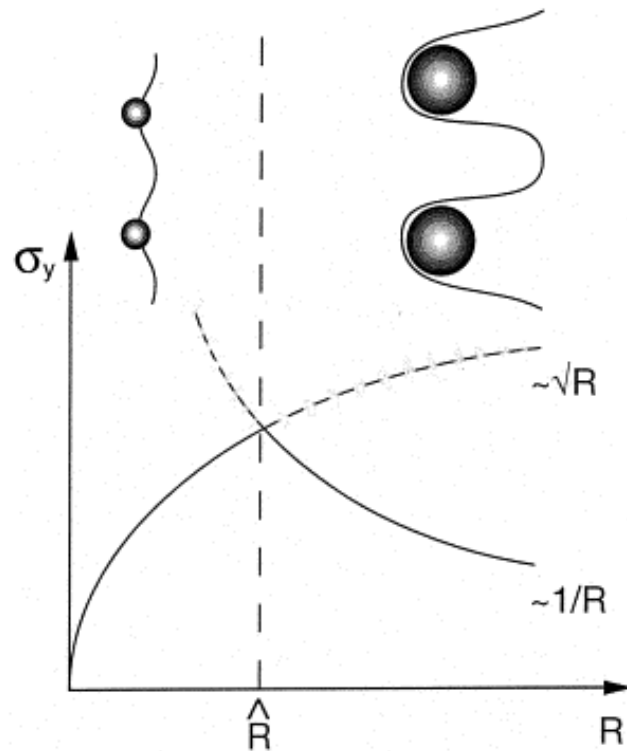


Figure 3.9 – Relationship between particle radius and yield strength of a given material. The optimal strength is achieved at \hat{R} , the point where the curve for cutting ($\sim R^{1/2}$) and bypassing ($\sim 1/R$) meet [39].

Grain refinement: the relationship between strength and grain size is given by the Hall-Petch equation [42]:

$$\sigma_y = \sigma_0 + kD^{1/2} \quad (3.1)$$

where σ_y represents the yield stress, σ_0 the flow stress of a unreformed single crystal and D is the grain diameter. The constant k depends on the material and dictates the efficiency of the grain boundaries in slowing down dislocation movement. Grain refinement may be achieved on a composite as follows: depending on how the reinforcement is introduced into the metal matrix, recrystallization may occur. In such instances, particles may either aid the nucleation of new grains (known as *particle-stimulated nucleation* – PSN [43,44]) or inhibit grain growth by exerting a pinning force counteracting the driving force that makes grain boundaries expand (phenomenon referred to as *Zener pinning* [45]). The latter mechanism is responsible for keeping the grain size constant upon a heat treatment aiming phase

dissolution or precipitation [36]. Particle size is an important factor dictating the effectiveness of a given particle on the grain boundary arrest [46,47]. While they might be important for nucleation increase, large particles do not act strongly suppressing grain boundary movement. At equilibrium, the original Zener relation (also known as Zener-Smith relation) between matrix grains and second-phase particles radii is given by

$$R = 4r/3f_v \quad (3.2)$$

where R is the mean matrix grain radius, r is the mean second-phase particle radius and f_v is the volumetric fraction [48].

3.4. Friction-based processes

A friction-based process resorts to the heat generated between two rubbing surfaces to increase temperature and soften materials, which eases the processing. A moving hard tool and a stationary component (to be processed) generally comprise those rubbing surfaces. When contact occurs, friction generates heat, which raises temperature and reduces the mechanical strength of the stationary component, without disturbing the structure integrity of the tool [49]. As mechanical strength dwindles, the component can be deformed to the desired shape. Heat generation decreases with the mechanical resistance of the stationary surface. As the component approaches its melting point, friction itself cannot produce heat anymore [50], which leads to a temperature drop. Thus, under normal circumstances no friction-based process involves melting [49,50].

Among the friction-based methods, two in particular arise as the most studied and applied industrially: the Friction Stir Welding (FSW) and the Friction Stir Spot Welding (FSSW). Both the FSW and the FSSW are employed to weld components. The FSW consists in a hard, rotating tool that contacts the line separating two plates or components. The tool mixes the material from both sides, as it travels from one end to the other of the facing surface. In the FSSW, however, the rotating tool does not move in any direction but vertically. The components to be joined are placed

one on the top of the other. The rotating tool makes contact with only one component first, and drives through it until the other component is finally reached. In the FSSW, the tool also mixes materials from both components, but differs from the FSW since it leaves a single spot welded, in comparison to a welded line featured by the latter.

3.4.1. Friction Surfacing

Friction surfacing (FS) is also a friction-based process. One of its main characteristics is that instead of a tool, a consumable rod (also called mechtrode) is used to promote friction, which avoids problems regarding the tool wear appearing both in FSW and FSSW [6,7,51]. The origins of this process date back from the II World War period [52], remaining relatively distant from any scientific research until the final of the 1980's, when efficient solutions for surface reinforcement by friction-based techniques began to be studied [50].

Differently from the two friction-based process presented earlier, the FS process is not employed to join components together, but instead it is used to deposit coatings in solid state (Figure 3.10). This process involves frictional heat and severe plastic deformation, resulting in high process temperatures (still below the melting range of the materials), often leading to refined grain sizes and thereby improved mechanical properties of the coating material. The consumable rod deployed in this process can be either made of the same material as the substrate on where the coating will be deposited or made of a different material [53,54].

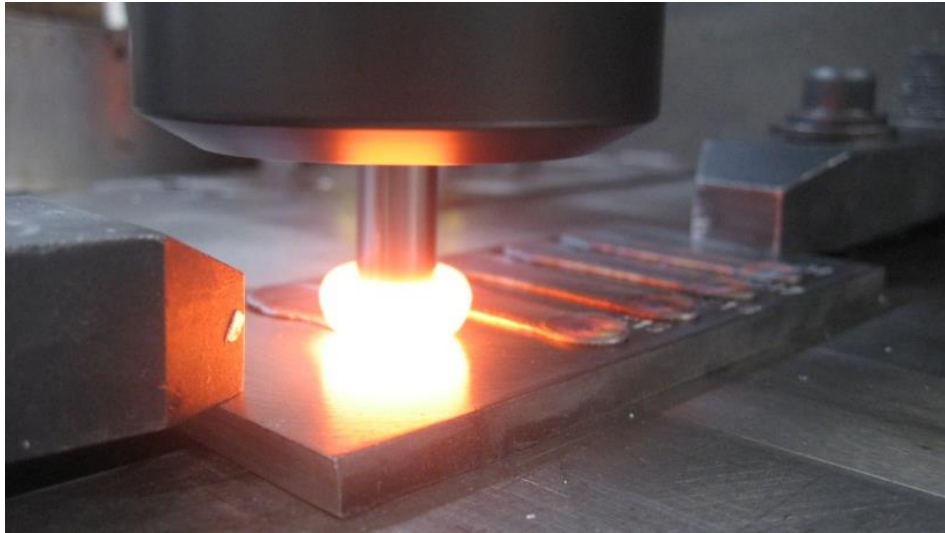


Figure 3.10 – Friction Surfacing process applying several successive layers of aluminum [55].

The stages of the process are schematically shown in Figure 3.11. Initially, a consumable rod is brought in contact with the substrate. The rod rotates and is pressed onto the substrate under a pre-set axial force (i). The combination of axial force and rotation in contact with the substrate generates friction and consequently heat, which leads to thermal softening and plastic deformation of the rod's tip (ii). Part of this “plasticized” material is squeezed out of the contact forming a “flash” around the rod. This results in shortening of the rod, which is recorded by the equipment used.

Once a pre-set rod length is plasticized, the substrate starts to traverse with a set deposition speed. As a result, plasticized material is deposited onto the substrate (iii). When the desired end position is reached or the rod is consumed up to its clamping, the remaining rod lifts off under rotation, thereby avoiding its welding onto the substrate (iv). The process exhibits an asymmetry, due to the superposition of a rotatory and a translatory movement. The coating side where the direction of the rotational velocity vector is the same as the deposition direction is defined as the advancing side (AS), and the coating side at which the rotational velocity vector is opposite to the deposition direction is defined as the retreating side (RS).

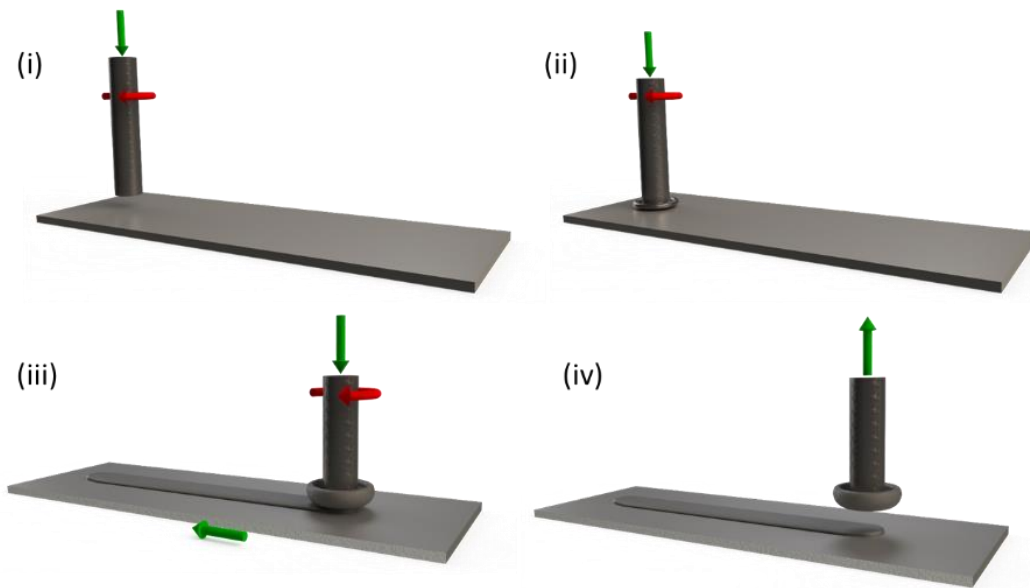


Figure 3.11 – Schematic depiction of the friction surfacing process showing different process stages acc. to [16].

The FS process allows to deposit different metallic materials, including aluminum alloys [56,57], steels [58–60], Cr60Ni40 [61], copper alloys [62] and cobalt-chromium alloys [63]. The generation of titanium alloy coatings by FS proved to be more complex compared to other reported metallic materials. This is mainly due to the tendency of flash formation at the coatings depending on process parameters such as deposition and rotational speeds [64], and a shift in material behavior and process characteristics at rotation speeds between 1000 and 2000 min^{-1} , resulting in two different deposition regimes [65], which is unprecedented in comparison to the FS of aforementioned alloys.

The deposition takes place as the material reaches viscoplastic behavior, which occurs at homologous temperatures between 0.5 and 0.9. This temperature range is reached by friction between the rotating consumable rod and the substrate [50]. The thermal gradient created between the region of the rod touching the substrate (hot) and a region not as much influenced by the friction (cold) leads to colder, hard regions applying torsion on hotter, softer regions [66]. As the rod material rotates and is pressed against the substrate, it can assume two routes: either go down and be part of the deposited coating or go up and form an aforementioned “flash”, surrounding the consumable rod with the shape of a ring.

Once part of the flash, the material does not actively participate on the deposition process anymore. Figure 3.12 shows the main material flow during the process [66]. Usually, the thermo-affected zone is smaller than the one present in fusion-based processes. This feature is result of lower process temperatures achieved during the deposition [66].

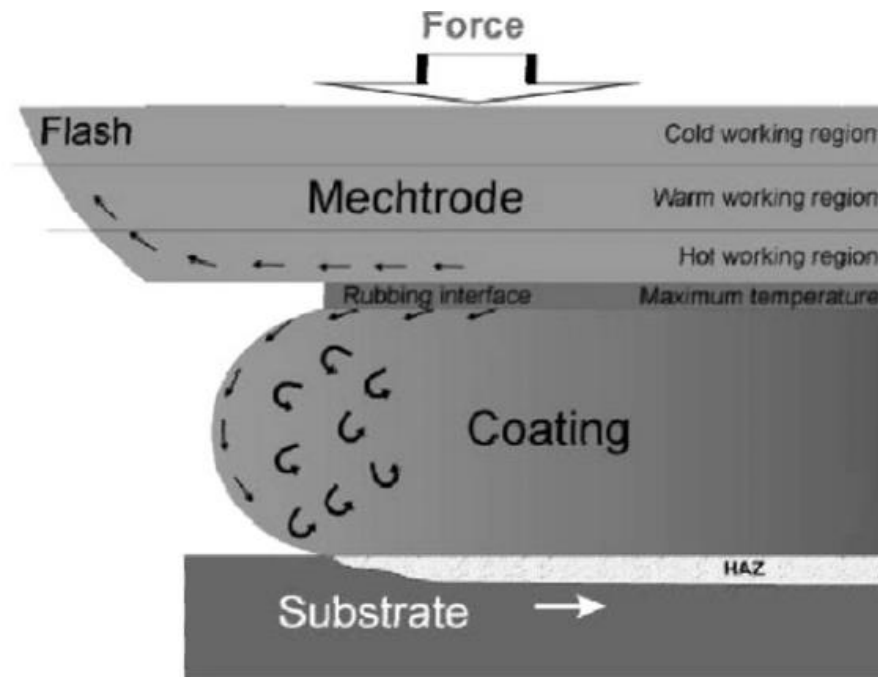


Figure 3.12 – Visual representation of the material flow during the FS. Adapted from [66].

Up to the moment, the most accepted hypothesis is that diffusion is responsible for the joining between deposited material and the substrate. Diffusion taking place during the process is not only related to the temperature, but to the axial force acting upon the consumable rod as well [66]. Another component that may aid the bond strength of the deposited layer is the interatomic forces, triggered by the short distances between contact surfaces. The latter hypothesis assume oxide layers being broken down during the process, which exposes the material bulk and eases the formation of new interatomic bonds. Nevertheless, the disruption of oxide layers upon the metal-to-metal contact during friction-based process has been proven possible by Shirzadi et al. [67].

During the process, there are three main controlled parameters, namely: rod's rotational speed (given in min^{-1} or rpm), traverse speed (mm s^{-1}) and deposition rate (or burnoff rate, given in mm s^{-1}), which represents the length of the rod consumed over a certain time interval. In order to keep a constant deposition rate, the axial force tends to vary along the process, according to the difficulty imposed by the rod material. The deposition rate may also be turned into a process response if one decides to control the axial force instead. In this case, the axial force remains constant, while the deposition rate varies [50].

The FS process has certain features that are frequently boasted as advantages in comparison to deposition techniques that rely upon melting [68,69]. For instance, the FS leads to refined microstructures devoid of defects and hard phases typical of processes where melting takes place [50]. However, it is important to emphasize that the FS shows important disadvantages as well, which have not been overcome to this date. After the process, coatings often present extremities of both advancing and retreating side not bonded to the substrate [70]; those areas need to be machined out in order for the deposited layers to be of any commercial value. Another problem inherent to the FS process is the low efficiency. Large portions of the consumed material usually end up surrounding the consumable bar, forming a waste called "flash", as previously mentioned [66].

The FS process could potentially be utilized to fix structures and on- and off-shore pipes in-situ [71,72], crack control in components present in nuclear powerplants [73], railroad repairs [74] and similar applications. Moreover, this process can also produce industrial and agricultural blades [15,75], knives [76], reinforced turbine dovetails [59], among others.

3.4.2. Manufacture of metal-matrix composites

Among several different techniques capable of manufacturing MMCs (such as powder metallurgy and casting techniques), friction-based methods have recently drawn attention. According to a 2012 patent, the FSW has been adapted to add a powder stream within the tool, which inserts at a controlled rate

a filler material into the weld [4]. Another MMC manufacturing method derived from FSW is friction stir surfacing [5], for which several holes are placed along the weld line (before the process) and filled with the reinforcement. As the rotating tool travels across the weld line, metal and reinforcement are mixed together, generating the composite [5]. The FSSW also offers the possibility of manufacturing MMCs. In this case, the reinforcement is inserted between the parts. The rotating tool makes contact with the metal-powder system, leading to particles being ultimately blended into the metal matrix [78]. However, an important obstacle for those methods is the rapid tool wear due to the high abrasive nature of the used particles [6,7].

According to several studies, the reinforcement of FS coatings with ceramic particles is not only possible, but may improve properties such as hardness and wear resistance as well. In 1994, Bedford et al. studied a case where different steels reinforced with Al_2O_3 particles were deposited by FS [8]. This study particularly compared wear rates of a low alloy steel (0.45% C) in two states: reinforced with alumina while deposited by FS and only quench-hardened. The results showed that the friction-surfaced coating had a wear rate over 6 times lower than the quench-hardened alloy, in spite of the latter being more than 20% harder than the former. In 2009, Reddy et al. reported the deposition of a previously reinforced AA2124-SiC composite material onto cast A356 alloy [9]. Two years later, Reddy et al. published another study, which aimed to deposit the same previously reinforced AA2124-SiC alloy on Ti-6Al-4V plates [10]. Improvements on wear resistance and hardness were reported on both papers, without any noticeable particle dissolution. In 2013, Gandra et al. published a study on depositing AA6082 layers reinforced with silicon carbide particles on AA2024 plates by FS [11]. Differently from the other studies, in this case the authors resorted to holes drilled on the consumable rod to introduce SiC particles into the process. The surface hardness of the reinforced layer was reportedly increased by up to 30% and the wear rate decreased by 13% in comparison to AA6082 layers without particles. Karthik et al. also used holes drilled on the aluminum consumable rod to add commercially-pure titanium particles into the deposit [12]. Published in 2016, this study performed the deposition of successive

layers of an AA5083 alloy on a fixed rod, which was made of the same material and had a slightly greater diameter than the consumable one. The authors observed that titanium particles were well distributed within the deposited layers, which led to fine, equiaxed aluminum grains in the matrix microstructure.

4. MATERIALS AND METHODS

4.1. Materials

As substrate material, Ti-6Al-4V (ASTM F 136-08) hot-rolled plates with dimensions of 300 mm x 100 mm x 10 mm were used. Consumable rods used were made of the same alloy, in a rolled condition with a diameter of 20 mm. The chemical analysis of the base materials was carried out and results are given in Table 4.1.

Table 4.1 - Chemical composition of the base material consumable rod and plate (wt. %)

	Consumable rod	Plate
Material	Ti-6Al-4V	Ti-6Al-4V
Fe	0.11	0.11
C	0.03	0.02
N	0.023	0.007
H	0.0039	0.0049
O	0.15	0.049
Al	6.6	6.2
V	3.5	3.9
Ti	Bal.	Bal.

Due to its stability during the process, titanium (IV) carbide powder (with molecular formula TiC) was the used as reinforcement for all the main experiments, i.e. where the process feasibility was studied. The size distribution of those particles was obtained by direct measurement of each particle resorting to images obtained by scanning electron microscopy (SEM) and is showed by Figure 4.1. Those results differed significantly from the datasheet provided by the supplier (99% > 4 μm), which justified the initial measurements.

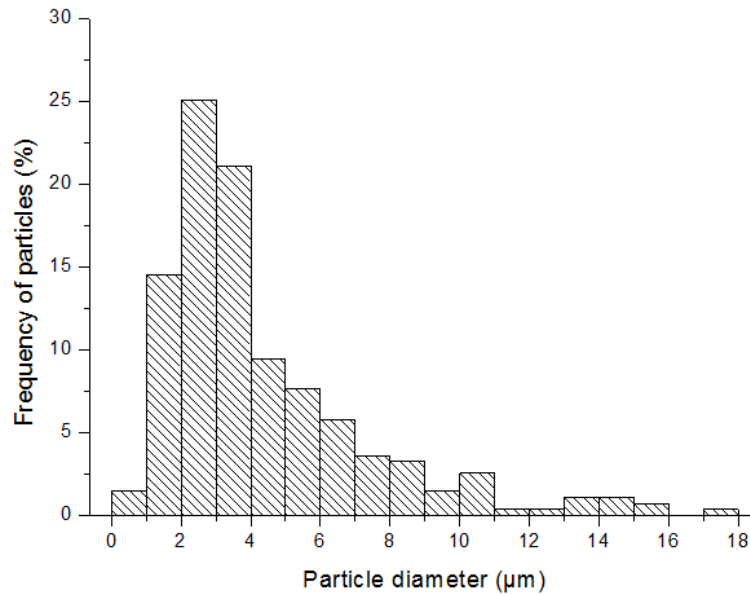


Figure 4.1 - Size distribution of TiC particles

In order to evaluate the consequences of adding other carbides as reinforcement particles to the coatings (in accordance with the minor objectives of this work), additional experiments were performed using silicon carbide (SiC) and boron carbide (B_4C), both with the same size (99% > 14 μm) according to the supplier.

4.2. Friction Surfacing process

4.2.1. Machine features

The present work resorted to a machine (Figure 4.2) that operates in three axes: the spindle (1) moves in z direction, while the table (3) is moveable in x and y direction. Table movement determines the welding direction, while the spindle movement controls the amount of material deposited. The rod (2) is attached to the spindle, whereas the substrate (4) is clamped onto the table.

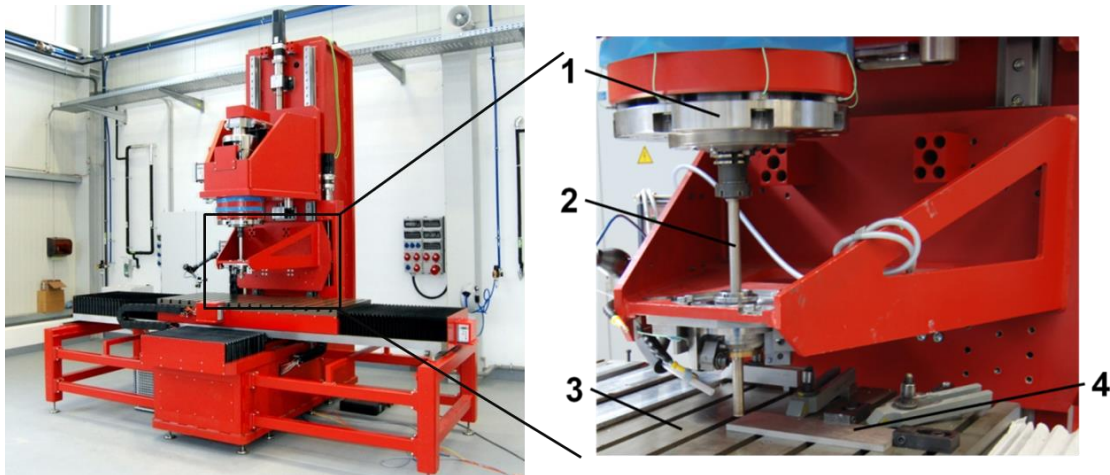


Figure 4.2 - Friction surfacing machine. 1) Spindle; 2) consumable rod; 3) moving table; 4) substrate (Helmholtz-Zentrum Geesthacht).

The axial force spans the whole range between 0 and 60 kN, while the rotational speed could be increased up to 6000 rpm. The electric motor of the spindle is able to keep constant rotational speeds, even at high torque peaks (which can be as high as 200 Nm). Sensors are placed in order to detect force in all three directions and the spindle torque. All the information is measured and recorded in a frequency of 100 Hz.

The machine is property of the Helmholtz-Zentrum Geesthacht, where all the coatings used for the present study were deposited.

4.2.2. Process parameters

The process parameters for the current study were used based on the publication of Fitseva et al. for deposition of Ti-6Al-4V alloy layers onto Ti-6Al-4V substrates [64].

During the initial plastification stage, an axial force of 9 kN was fixed. This force was kept until the rod shortened approximately 0.8 mm. From there on, the table started moving and the deposition stage commenced.

During the deposition stage, the rod was not pressed onto the substrate under a set axial force, as is commonly the case for FS. Instead, a constant axial

feed rate (“consumption rate”) was applied, and the axial force was therefore a resultant parameter, as previously explained. Further, keeping the rod consumption rate constant has the advantage that the consumed length of the rod during the process is always known, enabling to use exactly the rod depth containing the filler material particles.

All the experiments used to evaluate the process feasibility (with TiC) were realized with a rotational speed of 6000 min^{-1} , a rod consumption rate of 1.6 mm s^{-1} and a deposition speed of 16 mm s^{-1} .

For the experiments exclusively aimed to observe particle behavior (with B_4C and SiC), the same process parameters as the main experiments were applied, with exception of the rotational speeds, which were 3000 and 6000 min^{-1} .

4.3. Hole configurations

To reinforce the consumable rods with ceramic particles, holes were drilled according to the schematic (for one hole as an example) shown in Figure 4.3. The use of holes to insert particles into the consumable rod was based on the aforementioned study of Gandra et al. where aluminum coatings were reinforced by SiC particles [11]. To realize the desired coating length of approximately 150 mm with process parameters at the aforementioned values, roughly 15 mm of the rod must be consumed. Therefore, the holes were manufactured to an according depth of 15 mm. The diameter of the holes was set to 2 mm, since this dimension was large enough to enable one to insert manually the particles into the drilled cavity with relative ease, while small enough to represent only 1% of the rod’s cross-sectional area. About 14 mm of the depth were filled with ceramic particles, and Ti-6Al-4V wire was pressed into the remaining 1 mm of the hole as a closure.

For the feasibility experiments (with TiC), the number of holes (1 to 3) and their arrangement was varied according to Figure 4.4. For the particle behavior experiments (with B_4C and SiC), only one hole was drilled per consumable rod at 5 mm (configuration 1-B, see Figure 4.4).

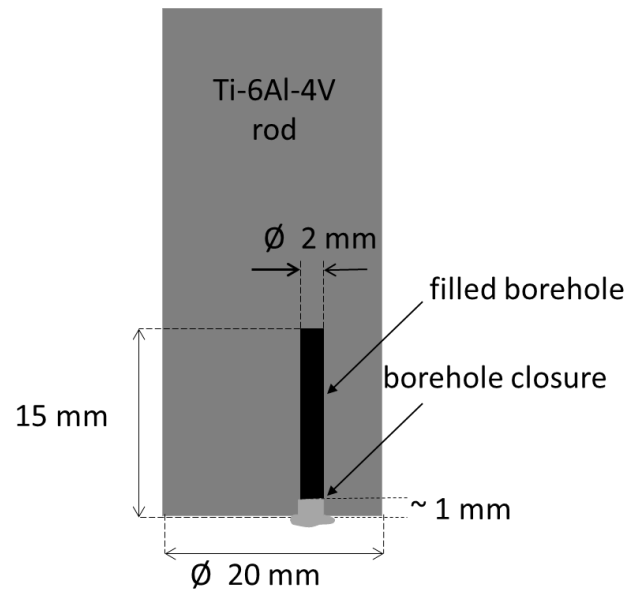


Figure 4.3 – A schematic of the reinforcement of Ti-6Al-4V rod (longitudinal section) with TiC particles.

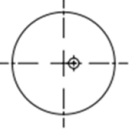
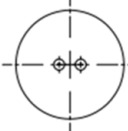
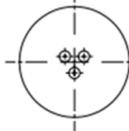

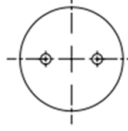
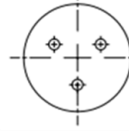
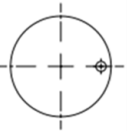
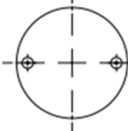
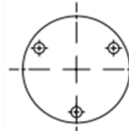
Distance to the center	Radial Position	Diametral Position	Y-Position
2 mm	 1-A	 2-A	 3-A
5 mm	 1-B	 2-B	 3-B
8 mm	 1-C	 2-C	 3-C

Figure 4.4 - Experimental design deployed to evaluate the process feasibility. Inside each hole, TiC particles were inserted. Each condition was labeled with a code, which is displayed next to the drawings.

4.4. Temperature measurements

Temperature measurements were carried out to relate microstructural features of the coatings to thermal phenomena. The process temperature was measured using thermocouples set according to Figure 4.5. Temperatures were registered with a frequency of 100 Hz.

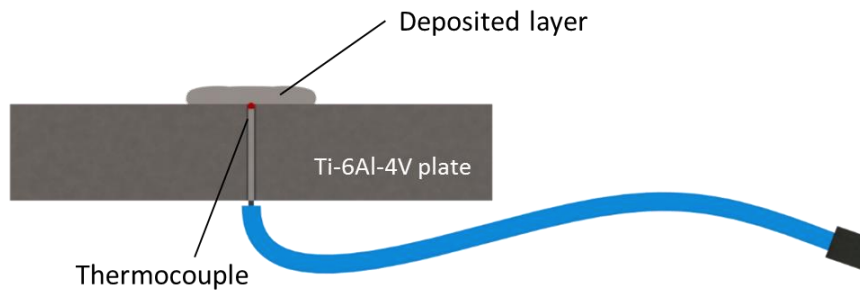


Figure 4.5 - A schematic of the thermocouple placement used for temperature measurements during the deposition process

4.5. Evaluation of coating quality by visual analysis

Following their deposition, coatings were evaluated by visual analysis. This analysis was deployed to determine the coating quality, and took into account the following items (in no particular order):

- (i) Coating uniformity (ideally, coatings should be as straight as possible on both AS and RS);
- (ii) Presence of poorly deposited sections;
- (iii) Presence of cracks;
- (iv) Particle loss to the immediate surroundings.

4.6. Metallographic sample preparation

For each experiment, transverse cross sections of deposited layers and the substrate were extracted from: (1) the first 50 mm deposited; (2) the middle

of the coating; (3) the last 50 mm. The preparation followed standard metallographic procedures. The samples were grinded and polished and the cross sections were etched with Kroll solution. The microstructure of the samples was observed with optical microscopes (Leica Microsystems DM IRM, Wetzlar, Germany; optical microscopes at DEMa - UFSCar) and with scanning electron microscopes (SEM) (Quanta™ 650 FEG and Inspect™ S50, both FEI Europe B.V., Eindhoven, The Netherlands) equipped with electron backscatter diffraction (EBSD) (Digiview IV CCD camera & TSL OIM Analysis 7, EDAX Inc., Mahwah, USA). For the EBSD measurements, an additional vibratory polishing step (VibroMet 2, Buehler, Illinois, USA) was applied for 12 hours, using 0.05 µm Silica suspension.

4.7. Hardness measurements

Microhardness measurements were performed on each feasibility experiment (with TiC), as well as on non-reinforced coatings produced with the same set of machine parameters. Tests were conducted using a BAQ UT 100 (BAQ GmbH, Braunschweig, Germany) hardness mapping machine with a HV0.2 scale. The distance between measurements was 200 µm, which surpassed the minimum of two and one half times the length of the diagonal of one impression (ASTM E92-17). The analyzed surfaces were the coating's cross-sections extracted according to section 4.6.

The data was processed using Microsoft Excel and Visual Basic for Applications (VBA) routines, according to the following steps:

- 1) Data exported from the machine to an excel spreadsheet. Hardness values from substrate and surrounding plastic resin were discarded. The result were matrices with rows and columns proportional to the actual cross section dimensions (factor of 200 µm).

Remainder hardness values were split into twelve blocks (Figure 4.6).

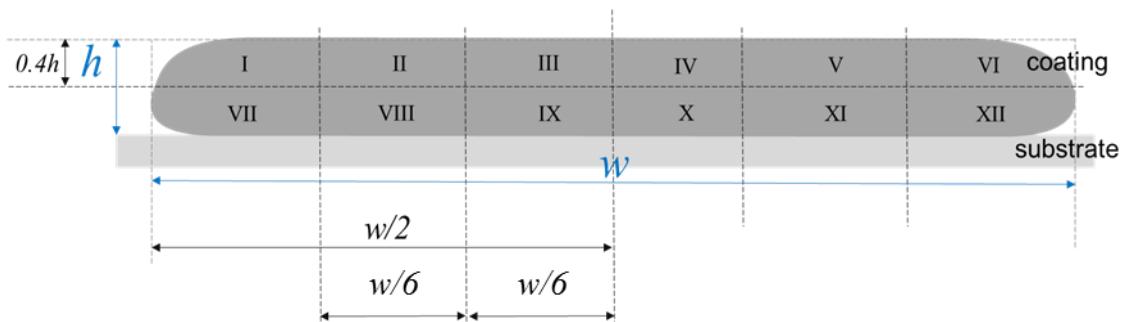


Figure 4.6 – Sketch of a generic coating divided in twelve blocks (labeled with roman numerals) according to the indicated dimensions.

- 2) A control group was established. This control group comprised samples from coatings deposited with identical machine parameters, but devoid of particle reinforcement. The treatment group, therefore, was represented by reinforced samples.
- 3) For each sample from the control group, an average hardness value was calculated for each one of the aforementioned twelve blocks.
- 4) For each sample from the treatment group, each value was divided by the average hardness calculated during step 4, depending on the block where the hardness value was situated. For instance, a value present within block II had its value divided by the average block II hardness (from step 4). The resultant hardness values composed matrices with same dimensions from the ones built on the step 1. Those matrices were also divided into twelve blocks, according to Figure 4.6.
- 5) The average value was calculated for each block, and was given in percentage points. For instance, the average value of 15% for the block VI of a given sample means that, at this particular location of the cross section, the hardness was, on average, 15% higher than the measured on a non-reinforced sample on the same area.

5. RESULTS AND DISCUSSION

5.1. Influence of hole configuration on coating appearance

Figure 5.1 shows the hole geometries with their respective resulting coatings. Irregularities in coating appearance were observed, which mostly included lack of deposition, deposition in a non-straight line and particle loss. The distance between hole and rod center had pivotal importance on the general coating appearance. Experiments with 2 mm distance led to irregular coatings, which became increasingly more regular as the holes moved away. The number of holes within a certain distance only magnified the effects. An increase in particle content in the rods was also reported to be detrimental to the coating quality by [8].

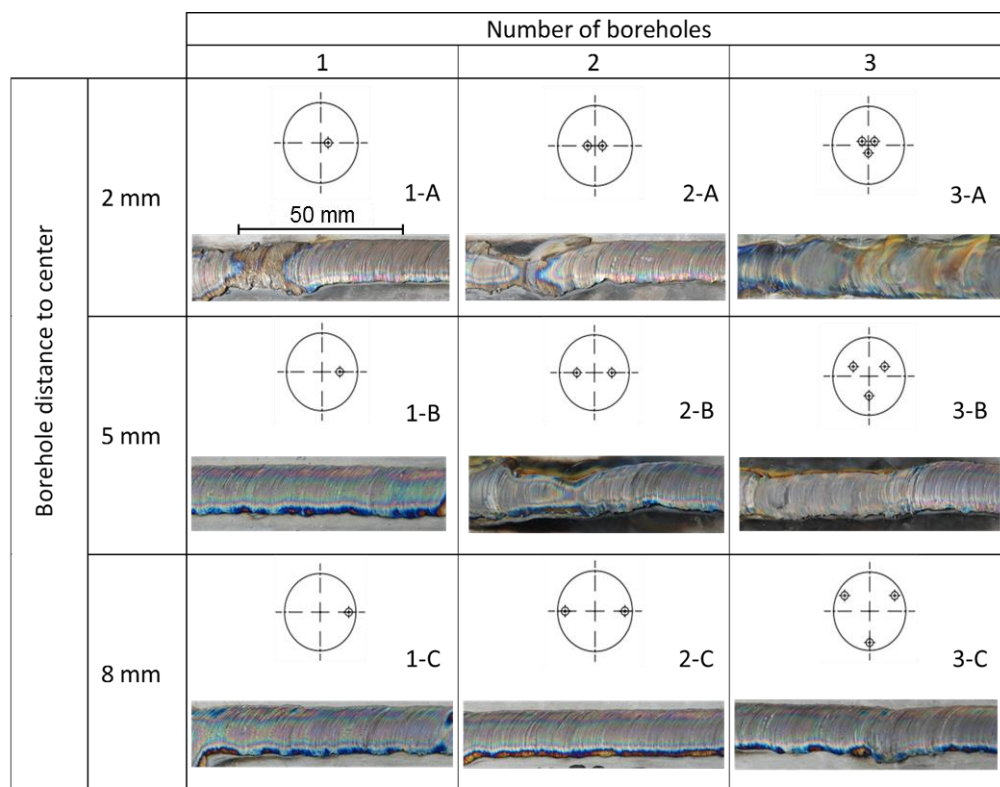


Figure 5.1 – Applied hole configurations and top view images of corresponding depositions. Configuration 3-A yielded an abnormally thin layer, comprised basically of oxides.

The deposition efficiency of the process is given by the ratio of deposited (approximately) to consumed material volume. The material fraction that is not deposited, i.e. the one that has a negative effect on the deposition efficiency, moves into the flash forming around the rod tip. The efficiency tends to decrease as the number of holes increases (Figure 5.2). This correlates well with the above described observations of the coating appearances. At 8 mm however, experiments displayed virtually the same deposition efficiency regardless of the number of present holes. In fact, the deposition efficiency for 8 mm experiments (around 37%) was close to the one reported for experiments performed with the same set of parameters, but without filled holes in the consumable rod (39%) [64]. Results showed that if placed within holes at 8 mm distance to the rod center, the particles show very little or no effect on the FS process behavior and the resulting coating geometry.

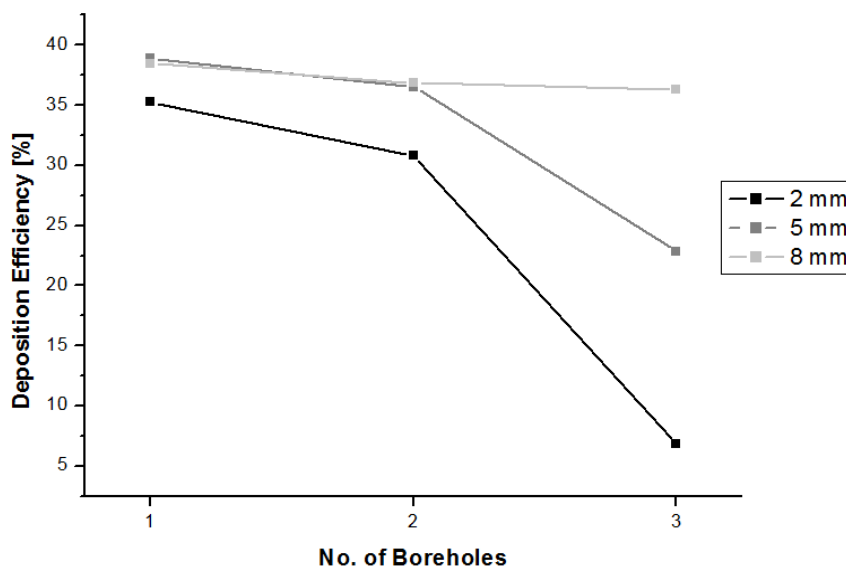


Figure 5.2 - Deposition efficiency calculated for the presented experiments.

5.2. Friction surfacing process response

During the initial plastification stage, a set axial force was applied to the rotating rod. In the deposition stage however, a consumption rate control mode

was used, i.e. a constant axial velocity of the rod was applied and the axial force was a resultant parameter (as described in section 4.2.2). It was reported by Fitseva et al. that the axial force varies with the rotational speed [64]. Since the rotational speed was not changed in the current study, it was expected that the resultant axial force would be comparable in all configurations. During the first FS trials with particles it was observed that very little shortening of the rod was achieved during the initial plastification stage (when axial force was fixed), requiring very long dwell times. Therefore, the axial force during this first process stage was increased to 9 kN, while FS depositions without particles are generally accomplished using 2 kN plastification force.

Axial force is plotted over process time for four FS process runs, one without particles, and the others each with three holes at a different distance to the rod center, as shown in Figure 5.3. In spite of the significantly higher plastification force, the rods containing particles still required more time. This plastification time increases with decreasing distance of the holes to the rod center. When the deposition stage sets in, the (now resultant) axial force drops and after a delay of a few seconds reaches comparable values as for the FS process without particles. Deposition run 3-A, with only 2 mm distance to the rod center, is an exception. Since here virtually no material was deposited (compare Figure 5.1), rod shortening was solely caused by squeezing out softened material into the flash and consequently the acting force remains very high.

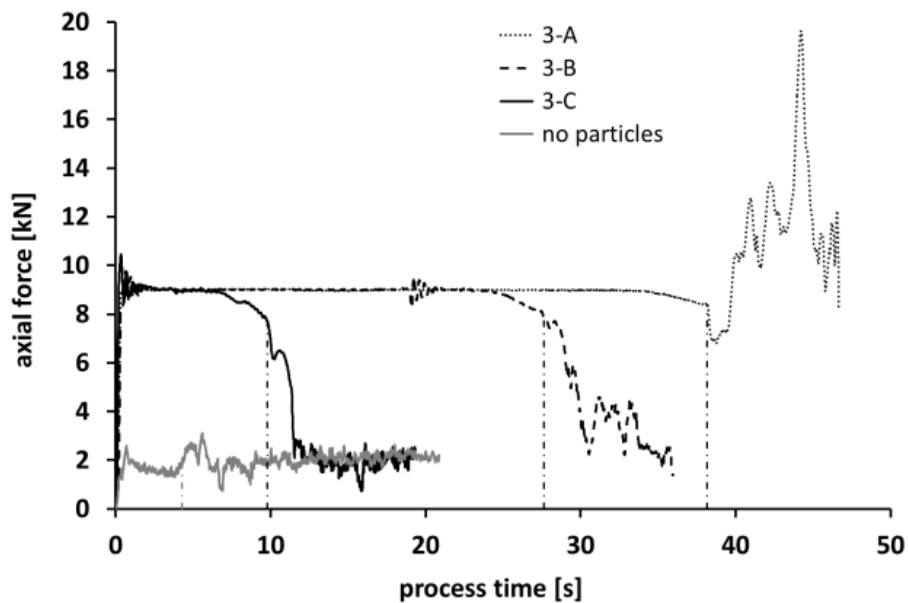


Figure 5.3 - Axial force diagrams for configurations 3-A, 3-B, 3-C and without particles. The vertical dashed lines indicate the transition between initial plasticizing and deposition stage for each condition after 0.8 mm rod shortening

The axial force of various process runs was plotted over the rod consumption in Figure 5.4. The depth of the filled holes was 15 mm, i.e. beyond that depth, Ti-6Al-4V without particles was deposited. The filled rods with holes at 2 mm distance to the center (upper Figure 5.4) all display higher axial forces than the plain rod up to a shortening of 10 mm, except again for trial 3-A, in which the deposited coating was abnormally thin.

Fluctuations of the axial force occur, which correlate with the irregular coating layer appearance. The value of approximately 2 kN, which acts constantly in the process run without particles is only reached after two thirds of the hole depth were already consumed (upper Figure 5.4). At this point, deposition became considerably smoother. However, cracks began to appear, perpendicular to the traverse direction (Figure 5.5). The process runs with holes at 8 mm distance (lower Figure 5.4) show higher axial forces than the unfilled rod only within approximately 3 s after the onset of the deposition state. This initially high axial force correlates with the time required by the equipment to speed up the axial velocity to the set speed of 1.6 mm s^{-1} . For the remaining deposition

process, axial forces of unfilled rods and those with holes at 8 mm distance to the rod center all ranged at the same value of ≈ 2 kN (lower Figure 5.4).

Process runs with holes 5 mm from the rod center (1-B, 2-B and 3-B) showed comparable force evolution as the ones with one or two holes at 2 mm distance (1-A, 2-A).

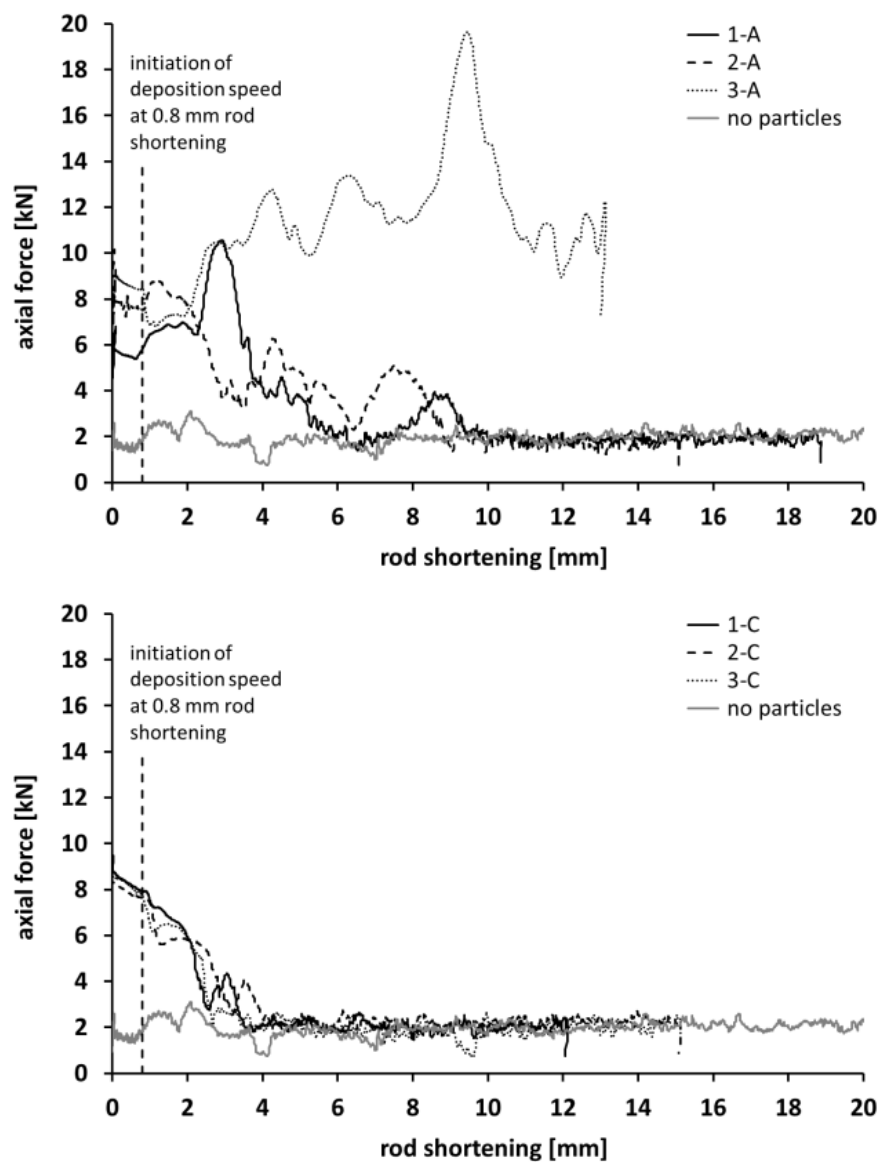


Figure 5.4 - Axial force vs. shortening of the rod (rod consumption) for 1, 2 and 3 holes at 2 mm (upper image) and at 8 mm (lower image) distance to the cross section center. Data from a deposition without particles is plotted in grey. The

vertical dashed lines indicate the transition between plasticizing and deposition stage.

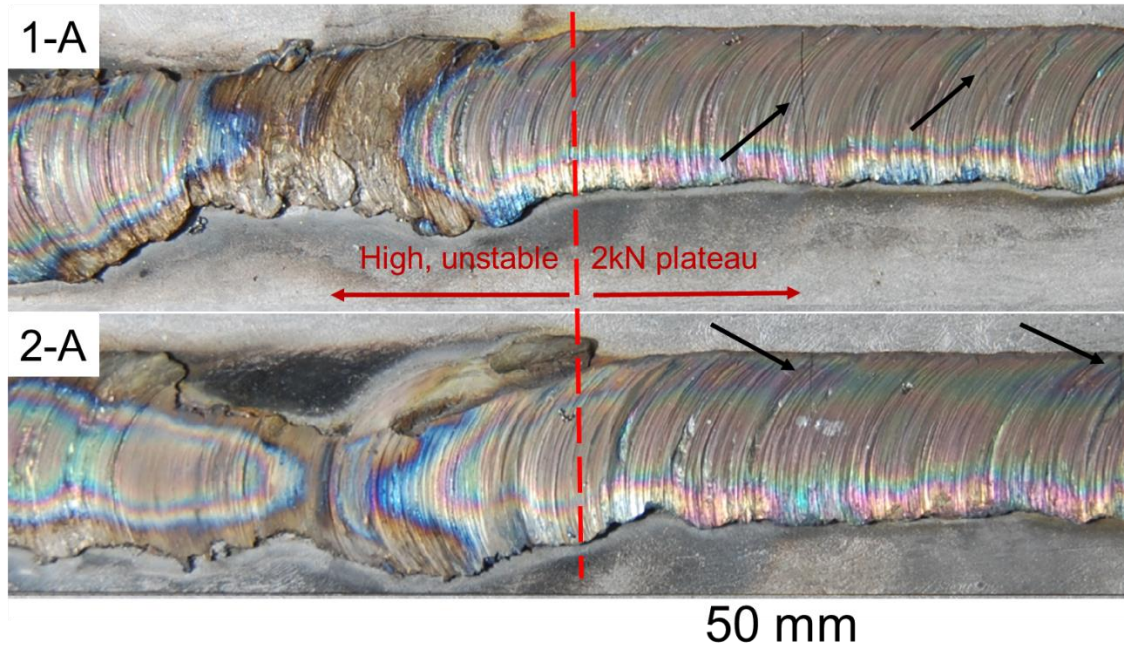


Figure 5.5 – Red dashed line represents the approximate transition from the deposition with high, unstable axial forces to the deposition with stabilized 2 kN. Black arrows indicate the present of cracks on the smoother portion of the coating.

The impact of the particles on the FS process is significant during the plastification stage, and less pronounced during the deposition stage. In the first seconds of the process, particles were visibly and quickly ejected from the initial rubbing interface. Since they move within the contact area, they may have two effects. Firstly, a layer of particles may separate the two metallic surfaces of the rod tip and the substrate, thereby hindering the adhesion between them, which is required for plastification. In a successful FS process, the rod tip is heated through frictional energy quickly and adheres to the substrate surface. The rotational relative motion is then accomplished by torsional shear of the thermally softened material within the rod tip, and further heat generation is achieved through viscous dissipation under plastic deformation [66]. If adhesion is hindered, the two components remain in a state of friction between the surfaces,

which may be less efficient at creating heat and result in longer plastification stages. Secondly, the particles may be able to roll and slip within the contact, thereby acting comparable to a solid lubricant in reducing the friction and with this the heat generation.

During the deposition stage only the particles in holes 2 and 5 mm to the rod center have a recognizable effect on the FS process. The force fluctuations and the irregular shape of the deposited layers imply that the particles cause instabilities in the heat generation and material flow. It can be further assumed that such instabilities are also causing the delay of initial plastification in those process runs. A higher amount of powder present intensifies these effects. During the periods in which the process runs as desired (depositing a thick layer of material) the particles are predominantly embedded in the soft, flowing metal surrounding them and are deposited with it. In these periods, sufficient heat generation is accomplished by the plastic shear deformation, and the axial force drops.

Hole configurations with large distance to the rod center present a very stable process behavior after the initial plastification stage. Any loose particles here may leave the contact quickly, since inertia (commonly referred to as “centrifugal force” in those situations) drives them out. In the center of the cross section, a direct metal-metal contact between rod and substrate may be possible with little disturbance from moving particles.

5.3. Particle distribution within the coatings

Figure 5.6 shows different deposition patterns when distance of holes to the rod center is varied (at constant number of holes: two). Samples were extracted from the middle section of the layer, when half of the coating was already deposited. At the edges of the coatings a lack of bonding can be observed, which is typical for FS and related to the inhomogeneous pressure distribution between the center and the edges of the consumable rod [11,66]. The particle distribution pattern is mostly parallel to the substrate surface, which

corresponds to the torsional shear flow of the plasticized rod material. Similar particle patterns of silicon carbide and tungsten carbide particles were also observed by Gandra et al. [11] and Rafi et al. [79], respectively.

As discussed previously, the hole placement exerted an important influence on the presence of particles within the coatings. In comparison to coatings generated from other conditions, particles were poorly mixed in for configurations with holes placed 2 mm off the center, remaining packed in large clusters. As distances increased, particles start to experience a pronounced scattering, which extends from the AS to RS. This led to a general decrease in particle volume fraction within the coatings.

According to Figure 5.6, particles take up 19% of 2-A's cross-sectional area, comparing to 10% of 2-B's and close to 0% of 2-C's. Further, the particle distribution allows drawing conclusions on the material flow, assuming that they flow along when they are incorporated into the softened Ti-alloy. Their location therefore leads to the conclusion that material from a 2 mm radius of the rod during deposition flows first towards the RS, and then partially back towards the AS as the rod continues to traverse (arrow in Figure 5.6, 2-A).

However, one must keep in mind that the material flow during FS is three dimensional, while the presented cross sections show only a 2D impression of it. Particles located at 5 mm distance off the rod center noticeably moves mainly to the coating surface and the AS, showing almost a negative image with regards to particle presence, compared to the cross section 2-A (Figure 5.6, 2-B). From the particles placed in holes at 8 mm off the center nothing or only very little was actually deposited (Figure 5.6, 2-C).

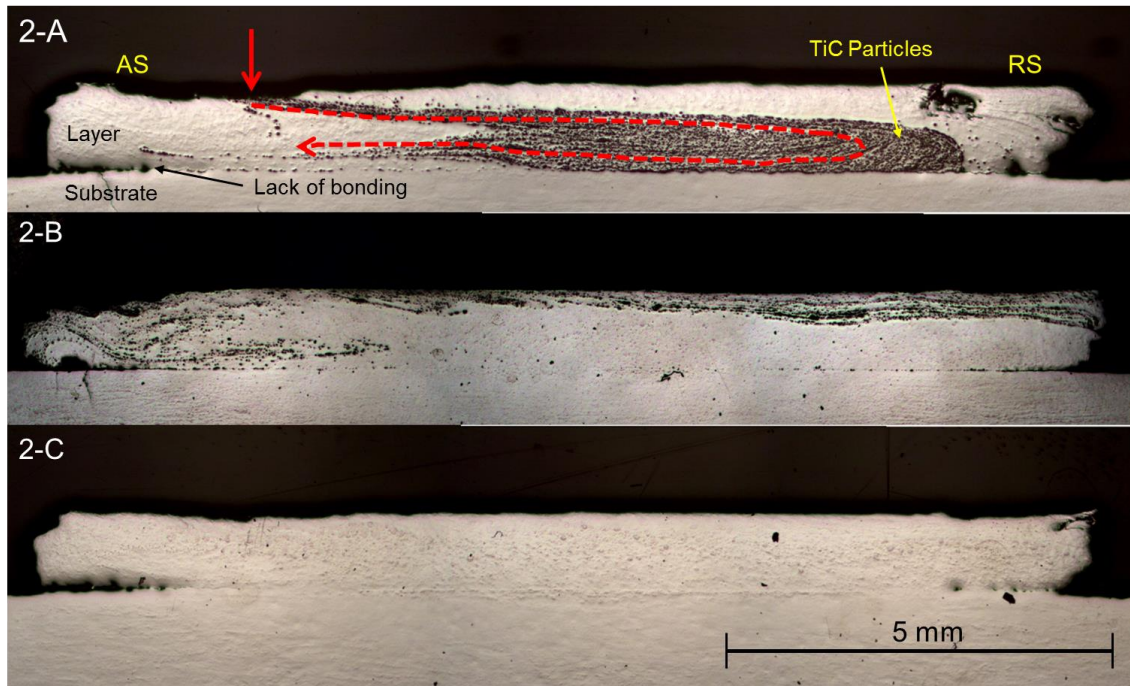


Figure 5.6 – Polished cross-sections from the middle section of 2-A, 2-B and 2-C configurations. A large agglomerate of particles is present at the inner regions of the 2-A coating, whereas particles are distributed sparsely near the surface and at the edges of 2-B coating. No particles are observed in 2-C coating.

During surfacing of configurations 1-C, 2-C and 3-C (8 mm off the rod center) very little particle ejection was observed. Instead, clusters of particles were found within the flash formed around the rod tip (Figure 5.7). It can be assumed that the high relative sliding speed between rod and substrate surface close to the outer circumference of the rod cross section results in intense heat generation and fast plastification.

Therefore, particles may be incorporated within the soft material efficiently, preventing them from being ejected. As the rod material from the radius of 8 mm is not deposited, but instead forms the flash, this hole location is not suitable to generate reinforced coatings with the process parameters selected in this study. In [64] for unfilled rods the highest deposition efficiency was reported for 3000 min^{-1} rotational speed.

Since the material deposited as coating in FS originates from the center of the rod, while surrounding material passes into the flash [80], it can be assumed

that even when changing the process parameters, particles from a hole location 8 mm from the rod center will not be deposited in the coating.

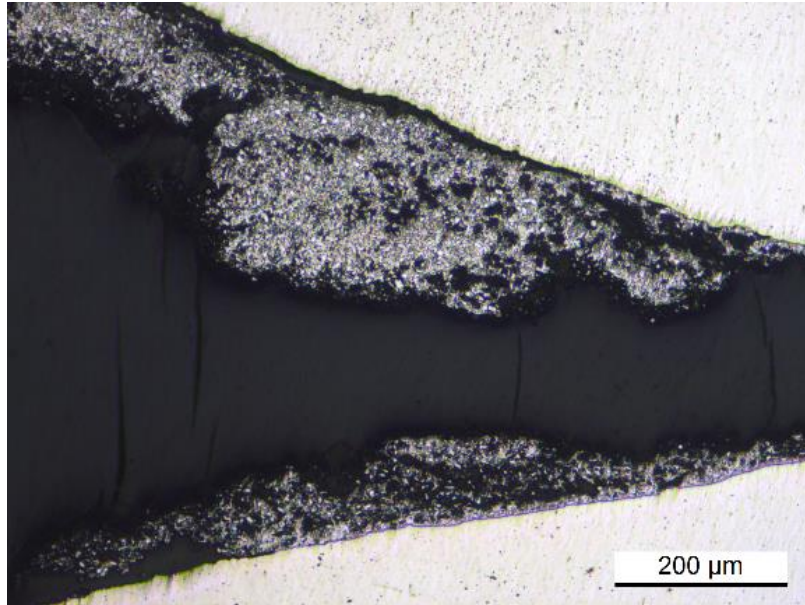


Figure 5.7 – Clusters of particles found within the flash formed around the rod tip during experiment with 1-C configuration.

Among the three different distances used in the present study, only the configurations with holes drilled 5 mm off the rod center offered the possibility of comparing thoroughly the amount of deposited particles according to the number of holes at a constant distance. This arises from the fact that 2 mm configurations did not effectively produce coatings for all sets of hole placements (3-A abnormally thin), in addition to 8 mm configurations not presenting any considerable amount of particles within the layers.

The comparison between 5 mm configurations showed an increase in particle presence from 1-B (Figure 5.8) to 2-B (Figure 5.6), with a mild decrease in deposition efficiency (Figure 5.2). No increase in particle presence was observed from 2-B to 3-B in spite of the latter condition containing an extra filled hole. Instead, while arguably 2-B coating presented an appreciable quantity of particles at the RS, 3-B coating shows much less reinforcement at that side, being densely reinforced by particles only at the AS (feature also appearing on 2-B).

Both configurations equally suffered with intense particle ejection (see Figure 5.1), although 3-B coating had less thickness and width than 2-B.

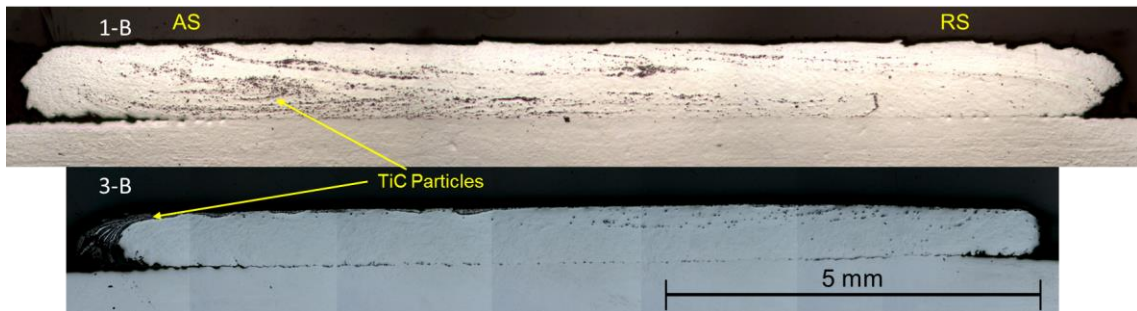


Figure 5.8– Cross-sections of 1-B and 3-B configurations extracted from the middle section of each coating. While configuration 1-B retained less particles in comparison to 2-B due to fewer holes on the rod, configuration 3-B did not present an increase in reinforcement density in comparison to 2-B.

Particle distribution patterns along the length of the same coating were not uniform in most cases. At the beginning of the deposition stage, particles tended to be concentrated on the RS, with considerably lower amounts deposited in other frequent deposition sites, such as the top surface and the AS.

After approximately 4 to 5 cm of deposition length was achieved, the deposition patterns gradually stabilized, resembling what is displayed by Figure 5.6 and Figure 5.8. Such a tendency may be associated with the axial force during the process. At the first seconds, while the axial force was dropping to a 2 kN plateau (Figure 5.3), it was still higher in comparison to the axial force applied on the remaining process.

Due to the high axial force, coatings were thinner close to the start, comparing to regions deposited with stabilized 2 kN axial force. For instance, 2-B coating was 27% thinner at the deposition beginning, whereas in the 2-A coating, where the axial force took considerably longer to drop to 2 kN, this difference was 67% (compare Figure 5.6 to Figure 5.9).

The decrease in coating thickness with the axial force was reported also by Gandra et al. in the FS of aluminum alloys without particle reinforcement [54]. As discussed in section 5.2, the particles initially act to reduce adhesion and friction by moving freely within the interface between rotating rod and already deposited material, and thereby limit the heat generation. In this early process stage, they are not well incorporated into the plasticized metal, and therefore few particles are present within the coatings, mainly on the RS and a small amount close to the coating surface.

As the Ti-alloy heats up and a larger volume is plasticized, particles are accommodated by the soft metal and start to follow the material flow to a greater extent, accompanied by a reduction in the required axial force. From the middle to the end of the coating length, the particle distribution remained virtually unchanged, as the applied axial force oscillates around 2 kN.



Figure 5.9 - Cross-sections extracted from the beginning of the coatings generated by 2-A configuration. The cross-sectional area is noticeably lower than the ones observed on samples extracted from the middle section of the coating, which is a product of a lower deposition efficiency during this stage of the process.

5.4. Microstructure evolution

Figure 5.10 shows the process temperature measured using thermocouples during a deposition in configuration 1-B. At the moment when the thermocouple is directly beneath the rotating rod the temperature peaks at 1127°C, dropping to 783 °C one second later (therefore with a cooling rate of approximately 340 Ks⁻¹ over that span).

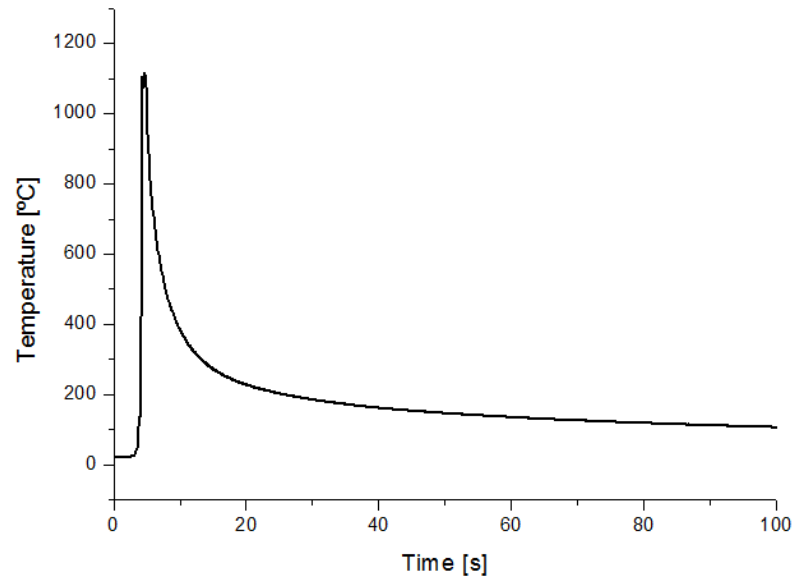


Figure 5.10 – Typical temperature evolution during deposition (configuration 1-B). In this case, peak temperature is 1127°C.

Ti-6Al-4V contains both hcp alpha and bcc beta phase at room temperature. At a temperature of 995°C, the alpha phase transforms to beta, so that the alloy is single phase at elevated temperatures [17]. At the measured FS process peak temperature, therefore a fully bcc lattice is existent. Due to the aforementioned high cooling rates, partially martensite formation occurs [81], in addition to the evolution of a Widmanstätten type of alpha, which is typical for Ti-6Al-4V [17]. The typical microstructure of a coating, in a location displaying no ceramic particles, is shown in Figure 5.11.

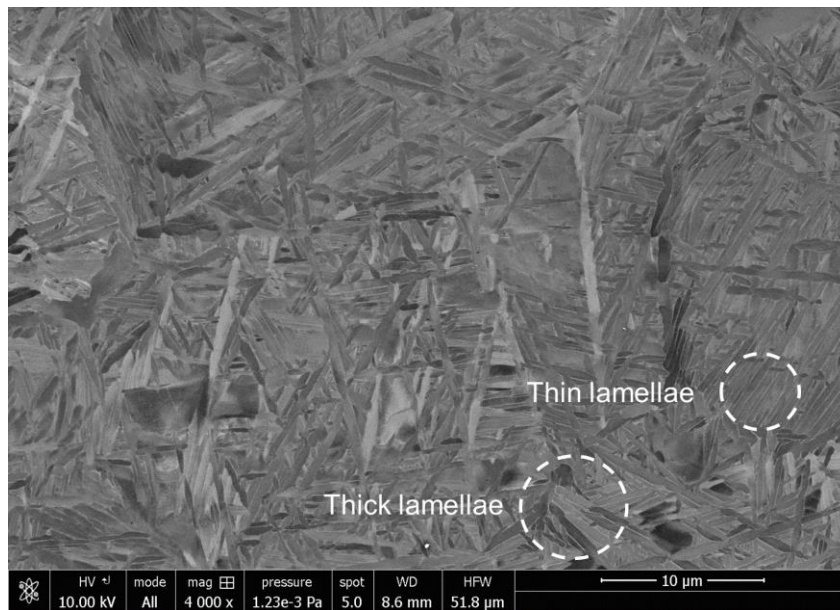


Figure 5.11 –SEM (backscatter electron) images of the coating microstructure. The Ti-6Al-4V matrix displays Widmanstätten or martensitic alpha lamellae.

Locally, small, equiaxed grains are visible (Figure 5.12). The equiaxed grains were observed appearing as trails, mainly parallel to the rotational shear plane. They were identified by EBSD as alpha phase, and they display mainly high-angle grain boundaries (Figure 5.13-a). Moreover, in the vicinity of the refined grains colonies of lamellae of equal orientation prevail (Figure 5.13-b). This indicates the local presence of alpha phase from massive transformation, instead of martensite or Widmanstätten type [82].

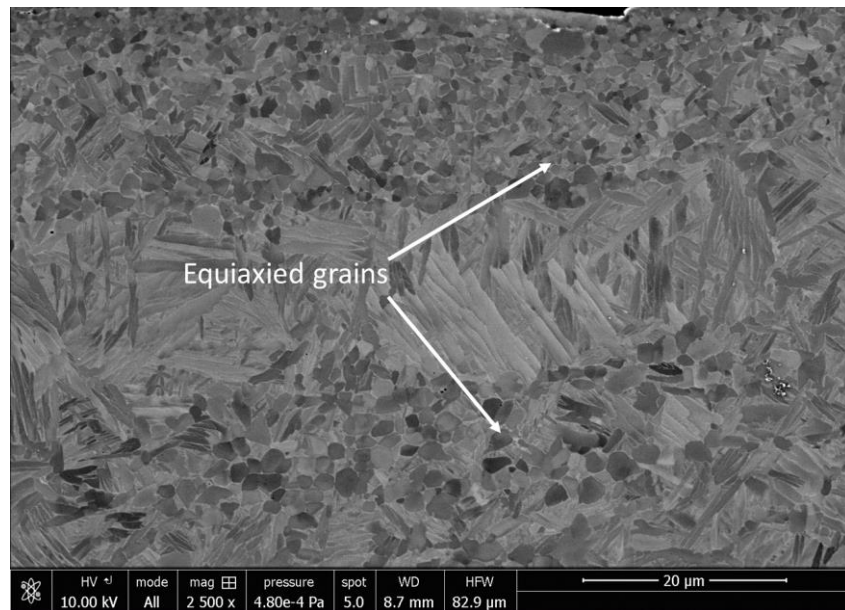


Figure 5.12 - Regions containing small equiaxed grains (mostly between 1 and 2 μ m).

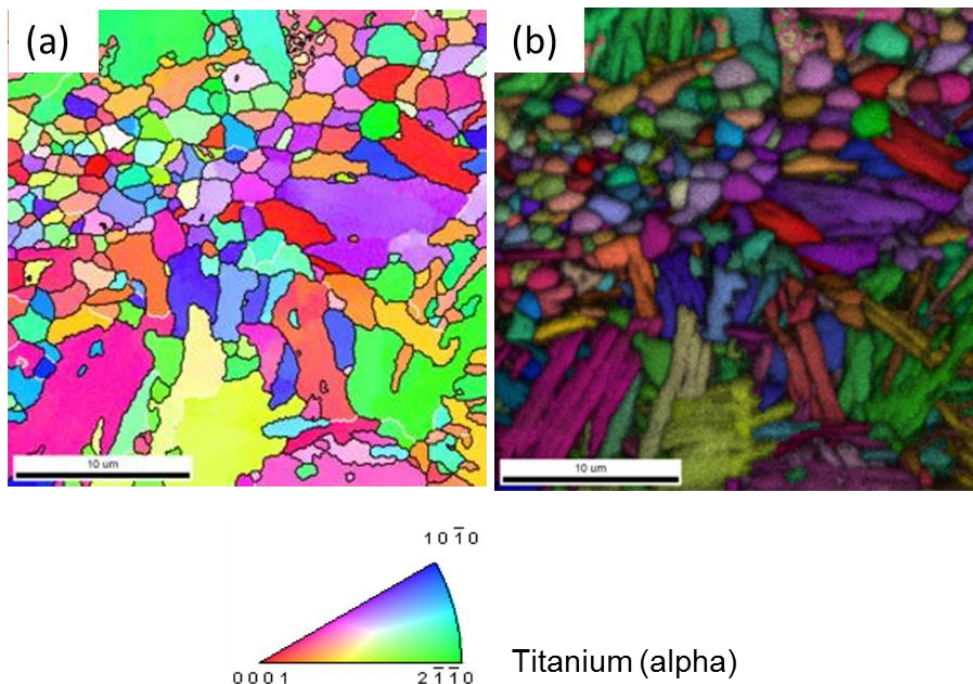


Figure 5.13 – EBSD image revealing fine equiaxed alpha grains surrounded by large grains. High-angle (black) and low-angle boundaries (white) are highlighted (a). A hybrid image of the inverse pole figure and the image quality is presented in (b).

The formation of bands of fine, equiaxed alpha grains was observed in titanium alloys processed by other thermo-mechanical techniques, and is frequently attributed to the occurrence of shear bands [83–86]. Such a phenomenon does not depend upon the presence of reinforcement particles. The possibility of shear band formation in Ti-6Al-4V at high temperatures was discussed by Seshacharyulu et al. in a study where that alloy was deformed by compression at several different temperatures and strain rates [87]. In that particular study, it can be observed that for strain rates greater than 1 s^{-1} , the compression at 1100°C revealed oscillatory stress-strain flow curves, credited to unstable deformation. In turn, such instability was credited to shear bands, found upon microstructural analysis. It is therefore reasonable to assume that such flow instabilities may also affect the FS process, whose peak temperature reached 1127°C with a strain rate of up to 10^2 s^{-1} .

Shear bands constitute regions where the dislocation density is much higher than in their immediate surroundings. Such a high dislocation density reduces the activation energy for the nucleation of the alpha phase during cooling along those regions. As a result, nucleation of the alpha phase within such regions is intense [88,89], and thus the microstructure along shear bands is refined (Figure 5.12), with grains between $1 \mu\text{m}$ and $2 \mu\text{m}$ in size. The characteristic distribution in the shape of bands allows to partially visualize the material flow during the FS process, which otherwise would be concealed by the phase transformation into lamellar alpha [88].

Due to the small grains, shear bands were measured with hardness approximately 41% higher than elsewhere (the relationship between hardness and microstructure will be thoroughly addressed by section 5.4.1). However, an important feature, frequently associated with the presence of shear banding and crucial to the mechanical performance of the material, is the occurrence of voids along the referred microstructures, as reported by Xue et al. for Ti-6Al-4V specimens [90]. In each one of the experiments performed for the present study,

shear banding occurred, frequently with the presence of voids, which can be observed surrounded by the aforementioned equiaxed alpha grains (Figure 5.14).

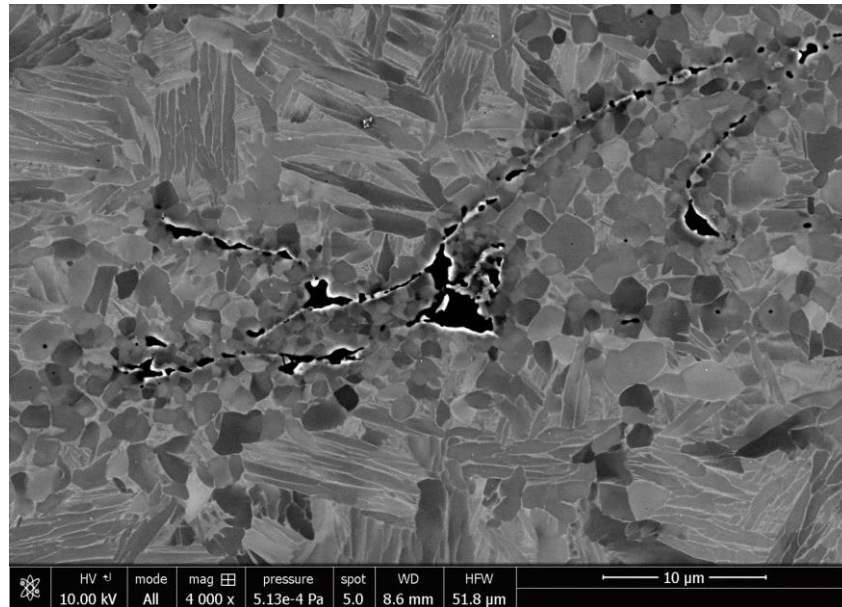


Figure 5.14 - Sequence of voids surrounded by equiaxed alpha grains.

Voids generally nucleated at alpha grain boundaries. While being individually only a fraction of a micrometer in diameter, those defects were observed merging one to another, provoking the formation of pores whose diameter could reach up to approximately 30 μ m (Figure 5.15). This is consistent with [90], where the possibility of void coalescence was pointed out.

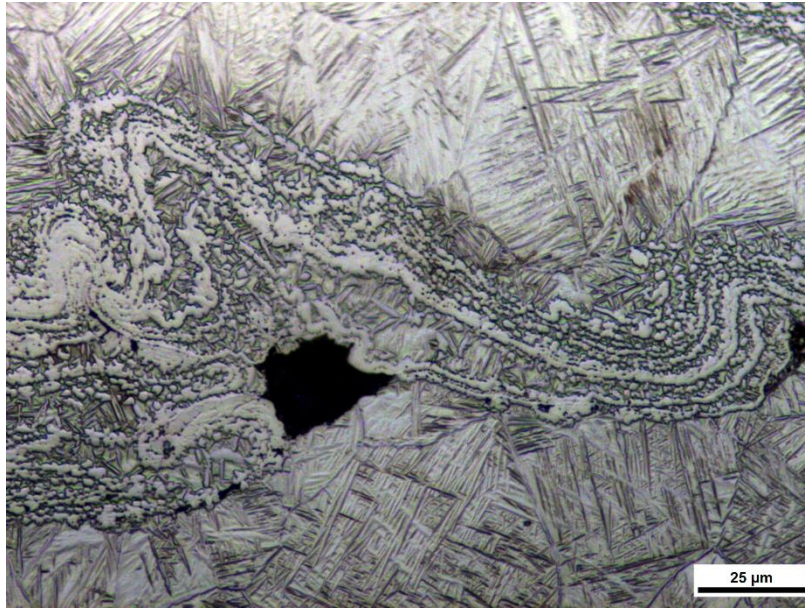


Figure 5.15 - OM image of an etched specimen where a trail of equiaxed grains can be observed slightly protruding over the matrix surface. Surrounded by that region is a pore with diameter of 34 μm .

Shear bands present within the deposited material are oriented predominantly parallel to the torsional shear deformation. This characteristic is shared by the particles' main deposition pattern. In the lower part of Figure 5.16 a trail of particles can be observed, above which a trail of fine recrystallized grains is located. This shows that the material flow occurred predominantly parallel to the shear plane not only within the presumed shear bands, but also in the surrounding alloy, thereby distributing entrapped particles in a similar banded shape. It is further visible in Figure 5.16 that the particle size strongly varies. The consequences of reinforcement particles being deposited along trails will be further discussed in the following section.

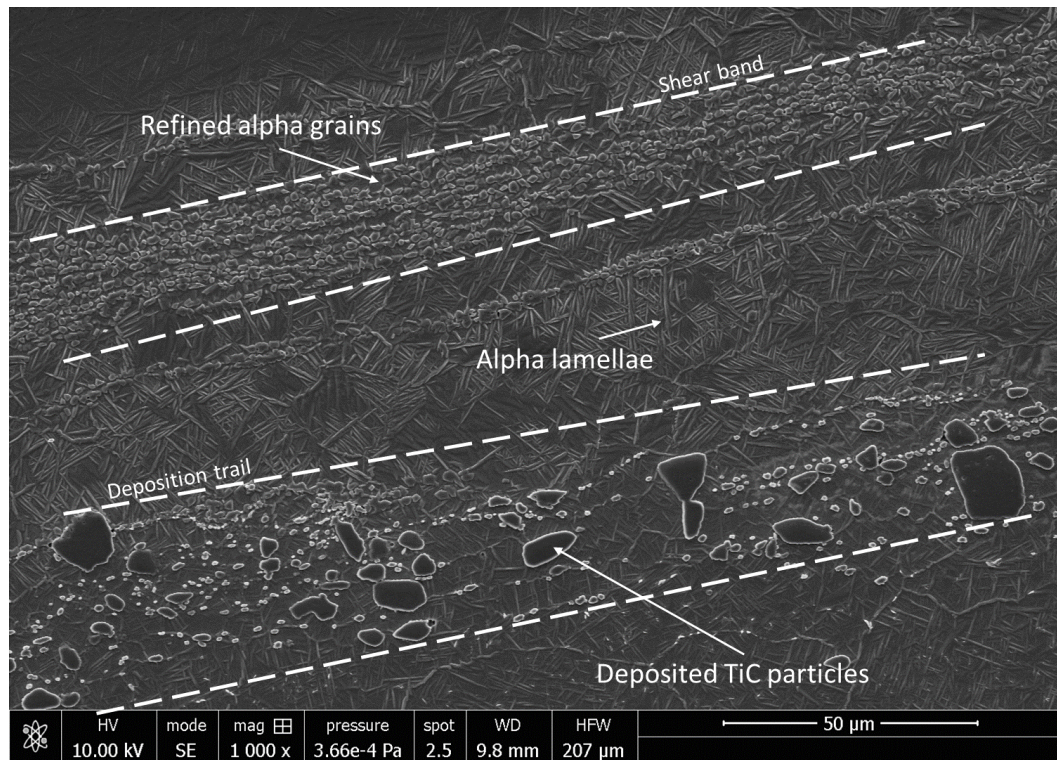


Figure 5.16 – Microstructure of a coating reinforced with particles (configuration 1-A). A trail of fine recrystallized α grains and a trail of deposited TiC particles can be observed in between which alpha lamellae are seen.

5.4.1. The influence of particles on dynamic recrystallization and its effect on coating hardness

As previously mentioned, the presence of embedded particles into the metal matrix induces several microstructural phenomena that have the potential to increase the hardness of a given material. As hardness increases, the likelihood of a proportional improvement of other important mechanical properties (such as tensile strength [91–93], fatigue [94,95], wear resistance [15,96], among others) increases as well, which makes hardness testing an important way to initially gauge the resultant characteristics from a mechanical performance standpoint of a manufactured material. This section will relate some microstructural characteristics regularly found on the FS coatings with their resultant hardness.

The OM image of a coating's microstructure (configuration 2-B) in Figure 5.17 shows a region containing particles located along prior beta grain boundaries. Since particle movement takes place only during the deformation, this indicates that the particles are involved in the recrystallization process of the material during the deposition. During dynamic recrystallization, the migration of high-angle grain boundaries occurs freely until a particle is reached, which locally hinders the further growth of the grain. Once the grain boundary and the particle surface are close to each other, the grain boundary movement over the particle is restrained since the particle exerts a drag force (usually referred as *Zener pinning* [45], as previously mentioned) against the grain boundary. This drag force of the particle counteracts the driving force, intermitting the grain boundary movement. Eventually, an extension of the grain boundary, as large as the diameter of the particle, is replaced by the surface of the particle.

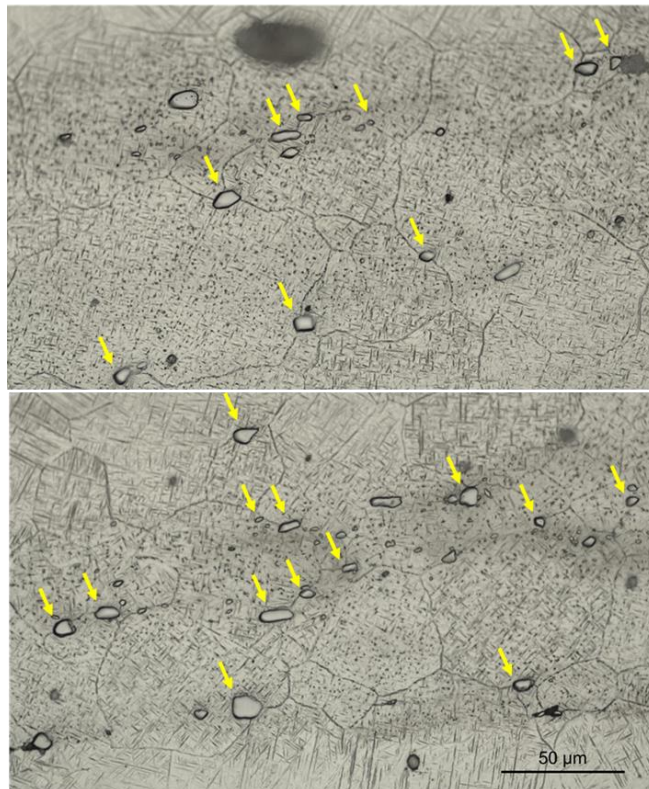


Figure 5.17 – OM photos showing examples of deposited particles embedded on the matrix (configuration 2-B). Yellow arrows indicate particles found at grain boundaries.

Particle size is an important factor dictating the effectiveness of a given particle on the grain boundary arrest [46,47]. In the present case, the size of the deposited particles, even after the process (where breakage may occur, which therefore would lead to a decrease in the average particle radius) is too large to arrest grain boundaries (2nd stage of the recrystallization). Instead, particles as big as the ones found on Figure 5.18 may aid the 1st stage of recrystallization, that is, the nucleation of new grains due to the dislocation field formed surrounding each particle. However, even in a scenario where particle size was appropriate to promote grain boundary pinning and therefore inducing smaller grains during recrystallization, the distribution of deposited particles within the recrystallized region is not sufficiently efficient to produce a considerable grain refinement. As already mentioned, particles tended to be concentrated within specific regions following the process, leaving the rest of the deposit devoid of any reinforcement. Moreover, even at particle-rich regions, the reinforcement was deposited mostly along trails (Figure 5.16 and Figure 5.18) and therefore not randomly. During recrystallization, grain boundaries were able to move freely only until reaching one of those particle trails, where the grain growth was halted. This kind of particle distribution is not as efficient for grain refinement as particles randomly dispersed across the matrix [47].

As a result of the ineffectiveness of a non-random particle distribution on grain refinement, regions devoid of particles and ones as rich in particles as in Figure 5.18 have very similar grain sizes: $22.0 \pm 5.0 \mu\text{m}$ and $20.5 \pm 10.4 \mu\text{m}$, respectively. Such a similarity carried over to the material hardness. After comparing hardness maps (obtained by the method described in section 4.7) with macrographs of reinforced coatings, no clear relationship between particle presence and hardness within certain area could be determined, as exemplified by Figure 5.19. Values mostly fluctuated within the standard deviation of measurements on the control group.

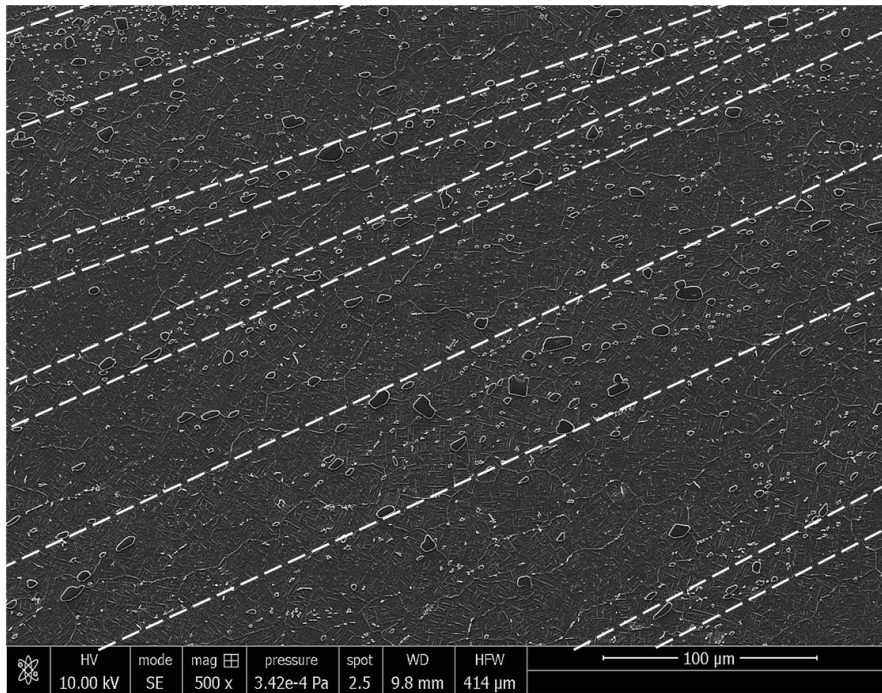
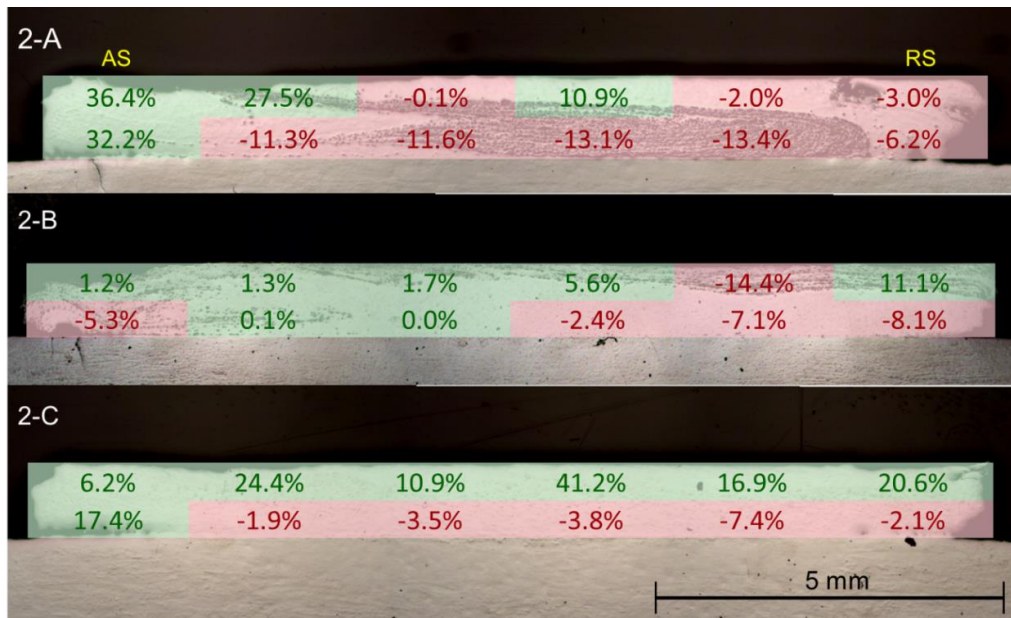


Figure 5.18 – Microstructure of the coating (configuration 1-A) shows TiC particles mainly deposited along trails delimited by white dashed lines.



AS				RS	
25,1%	29,4%	27,5%	25,2%	19,7%	37,1%
18,7%	5,3%	3,7%	1,8%	2,6%	45,1%

Figure 5.19 – Above, cross-sections of 2-A, 2-B and 2-C configurations and their relative hardness for each block, in comparison to regular, non-reinforced

coatings. Darker areas indicate the presence of particles. Below, the standard deviation for each of twelve blocks from measurements on the control group

Cases where relative hardness values stood beyond the standard deviation may be attributed to the high standard deviation of the measured grain sizes found on reinforced areas (close to 50% of the average grain size itself). However, that may not be the only factor contributing to abnormal results, as on some instances hardness measurements could be altered by reasons other than the local grain size. For example, in configuration 2-A (Figure 5.19), hardness values in an excess of 11% lower than the ones found on the control group were observed at the cross section's inner areas (blocks VIII to IX according to Figure 4.6), which had a particle density much higher than commonly observed on other samples.

Although this result may seem counterintuitive at first, areas with densely packed particles are prone to matrix cracking, which in the present case is largely potentialized by the high cooling rates (see Figure 5.10). This subject will be further discussed in section 5.4.2.2.

Another important occurrence at those particle-dense areas that might be decreasing hardness is the poor mixture between particles and metal from the consumable rod. As regularly occurred in areas with mild particle density, the metal from the consumable rod, very ductile due to the high process temperature, was able to be deformed in such a way that particles could be properly accommodate on the matrix. On the other hand, when a dense cluster of particle was flowing during the process, the lack of metal as sort of a "medium" whereby particles could move led to the emergence of pores (Figure 5.20), which would be filled in during the process if the metal/particle ratio was locally higher. Pores at the interface between coarse particles and metal matrix are observed on composites welded by FSW [97,98], being this phenomenon also attributed to a likely reduction of the material ability to flow in those scenarios [99].

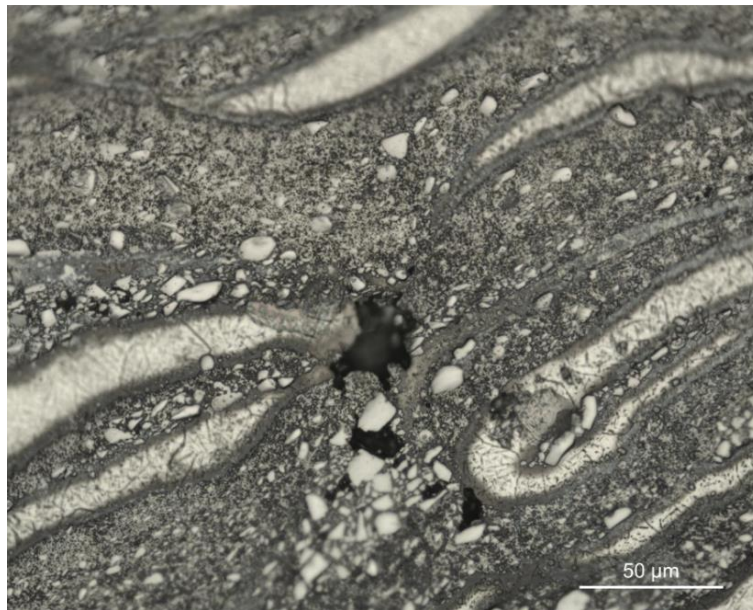


Figure 5.20 - OM photo of an area of very high particle density where pores can be observed. Configuration 2-B.

Cracks and pores among reinforcement particles alter hardness measurements in such a way that this kind of test is no longer able to reliably predict the real characteristics of the sample. In this case, the graphical representation of the probabilistic distribution of hardness measurements shifts from a bell curve, typical of a Gaussian (or normal) distribution, to a multi-peak curve, which is related to a multimodal distribution.

A multimodal distribution is frequently attributed to a system containing multiple, different populations, each with its own probability distribution. In the case of samples with densely-packed particles, different populations are mainly measurements on (or close to) pores, on cracks, on particles themselves, on matrix/particles and so forth, with each having its own probabilistic distribution. The comparison between the hardness values distribution of a typical particle-free configuration (with a single peak) and a particle-rich one (with multiple peaks) (Figure 5.21) is consistent with the presented hypothesis. Furthermore, in Figure 5.21 it is also possible to observe, once again, the irrelevance of particle presence on the overall hardness of the coatings, as previously demonstrated.

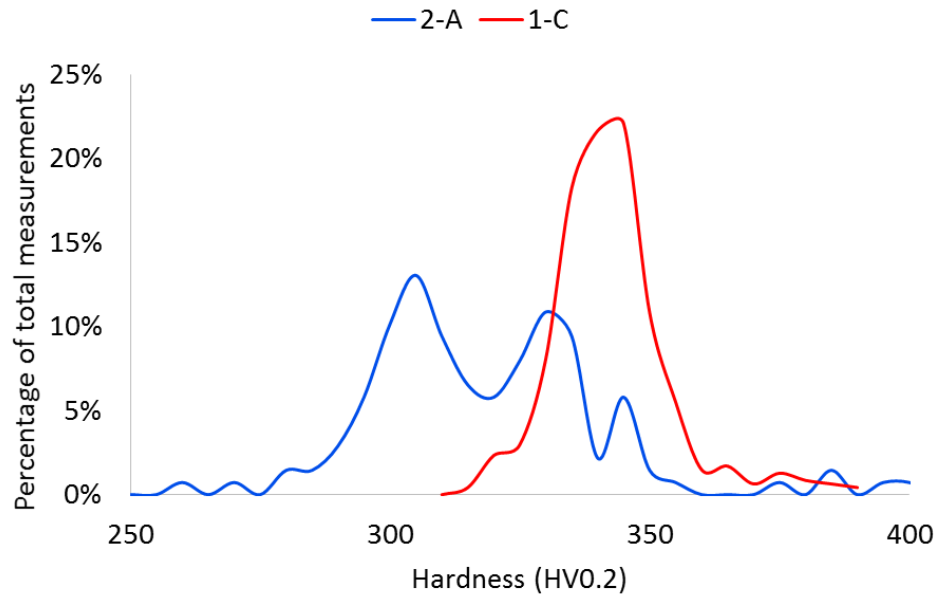


Figure 5.21 - Distribution of hardness values from inner cross-sectional areas of samples extracted from two different configurations: 2-A (particle-rich) and 1-C (particle-free). In order to factor out oxygen absorption by outer cross-sectional areas, only the inner regions of the coatings were evaluated.

However, it is important to point out that the low hardness measurements found on densely packed areas may not be necessarily result of cracks and pores. Since the reproducibility of the process was not subject of analysis on the present study, the possibility of the abnormal results being nothing more than a fluctuation around a real value is considerable. Pores and cracks do lower hardness measurements; however, the high quantity of particles should be able to overcome any drop in the hardness value resulting from anything else.

5.4.2. Particle behavior: dissolution and fracture

In this section, particles' behavior concerning their dissolution and breakage will be addressed. From here on, depositions using the covalent carbides B_4C and SiC as reinforcement are introduced, not to further evaluate the process feasibility and optimal parameters (where only the stable TiC particles

were employed), but instead to compare the different thermodynamic behaviors of different carbides during the process. As mentioned on the “materials and methods” section, it was expected that TiC would withstand the depositions without undergoing degradation. However, it was not clear if other carbides would remain undissolved in the same situation due to the short process time and high cooling rate, which possibly would make particle degradation not severe. In this case, particle dissolution would not be a limiting factor to the process and therefore more particle types could be deployed as reinforcement on an eventual industrial application of the FS process as studied here. This chapter aims to clarify this subject for the FS of titanium alloys.

5.4.2.1. Particle dissolution

5.4.2.1.1. Boron Carbide

B₄C reinforcement particles were observed dissolving into the metal matrix during the process, as evidenced by EDS analysis (Figure 5.22, Table 5.1). The dissolved atoms present in solid solution within the alloy matrix then proceeded to precipitate in other regions during the process, constituting different phases. Once diffuse into the metallic matrix, boron, carbon and titanium atoms can combine to form a new phase virtually anywhere. However, they are strongly forced to do so at regions with high free energy, e.g. grain boundaries, phase boundaries, around pores, regions with large dislocation density in general [100]. When a particle is not completely reacted, its surrounding deformation-field [35,101] exhibits high dislocation density and thus are favorable sites to promote this new phase nucleation. Moreover, foreign atoms coming from the boron carbide have to travel shorter distances to nucleate around the particles in comparison to anywhere else. As a result, layers of the new phase were found around the still-existing B₄C particles (Figure 5.22).

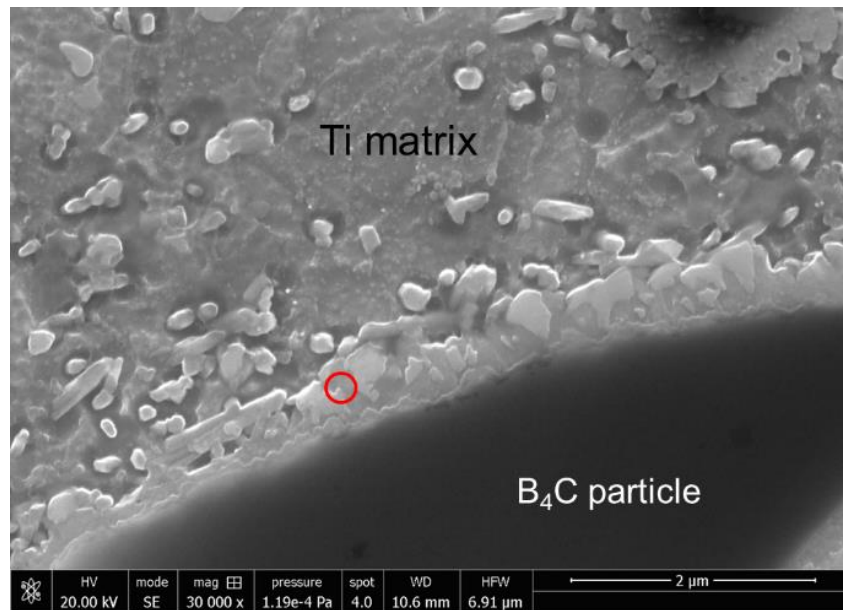


Figure 5.22 – B₄C particle embedded in Ti matrix by FS (rotational speed of 3000 min⁻¹). EDS analysis was performed on the area highlighted by the red circle.

Table 5.1 - Results of EDS analysis performed on the highlighted area indicated on Figure 5.22.

Element	Weight %	Atomic %
B	18.84	45.26
C	3.87	8.37
O	2.46	3.99
Al	4.48	4.31
Ti	67.48	36.60
V	2.87	1.47

At approximately 1400 K (roughly the peak temperature according to measurements, see Figure 5.10), no reaction is thermodynamically favorable between TiC particles and the titanium matrix, which explains the stability of that compound and thus the absence of reinforcement dissolution in such a case. On the other hand, titanium matrix and the B₄C particles, when in contact, may undergo two separate reactions, namely [102]:



Both reactions 5.1 and 5.2 are favorable from the thermodynamic standpoint due to their negative ΔG^0 . Moreover, even in comparison to other possible favorable reactions, (5.1) and (5.2) stand out as the ones associated with the lowest ΔG^0 (Figure 5.23). Kinetically, at the mentioned temperature, diffusion is boosted to the point that such reactions can occur even during the short process time.

Reactions 5.1 and 5.2 are exothermic (-795 and -752 kJ/mol respectively [102,103]). Despite the low reinforcement volume (approximately 0.04 cm^3 , which equals to 0.002 mol of B_4C), if all the B_4C of one hole reacted, it is estimated that the complete reaction would produce roughly 1.5 kJ . This is sufficient to increase the temperature of the coating itself (approx. 10 grams of deposited material) in almost 300 K , considering that all the generated heat was transferred directly to the deposited material. In practice, however, the temperature increase is not as high as the calculated one, since the generated heat ends up being transported also to the substrate, consumable rod, machine table, inert gas stream and so forth.

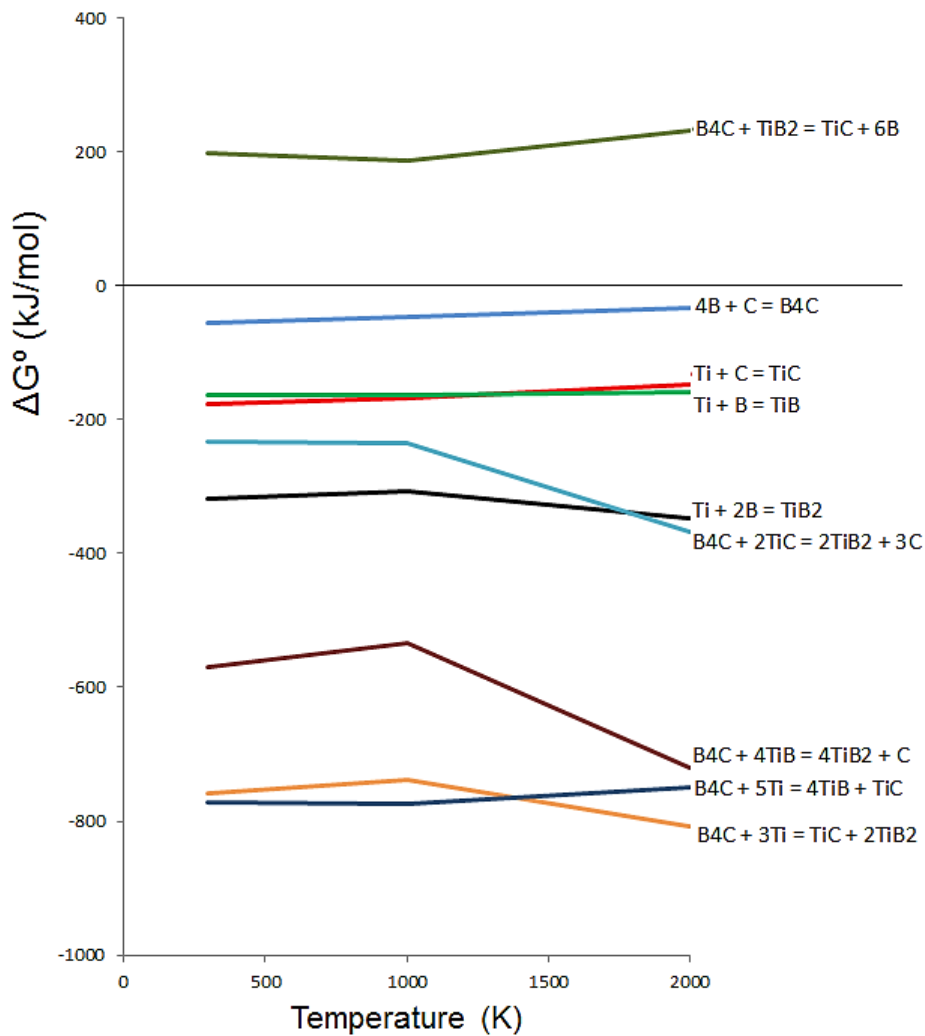


Figure 5.23 - Possible reactions involving boron, titanium and carbon, according to their Gibbs free energy of formation.

According to either (1) or (2), TiC was formed together with a boride (TiB or TiB₂). However, due to the much higher diffusivity (up to 10³ times [104]) of C in the Ti matrix in comparison to B atoms, TiC was the first component to be created. The contact between this compound and the B₄C particle (not yet totally dissolved) triggers another thermodynamically favored reaction:



Given enough time and temperature, the created TiC, when still in contact with the B₄C particle, tends to be consumed, generating TiB₂. This generated TiB₂

in contact with the B_4C particle does not react, since the reaction between both compounds is highly unfavorable (Figure 5.23). The data obtained from EDS analysis performed on the new-born phases found around B_4C particles projected on the Ti-B-C ternary diagram indicated the formation of TiB_2 (Figure 5.24) [105]. However, considering the limitations inherent to the EDS analysis and the reaction kinetics (which were not thoroughly studied here), there was an important possibility of TiC being still present around B_4C particles. Moreover, reaction 5.2 predicts the formation of TiB , which usually is produced in form of whiskers [106–108]. Such formations were also found around particles (Figure 5.25), albeit at a much smaller concentration. The low incidence of TiB whiskers in comparison to other newborn phases may suggest that reactions 5.1 and 5.2 rapidly took place, which created low quantities of TiB_2 and TiB and a high quantity of TiC . As TiC was produced, it wrapped the B_4C particle around, depriving it of contact with the Ti matrix and consequently making 5.1 and 5.2 halt. From this point, reaction 5.3 began to go off, whereby the majority of TiB_2 found was formed.

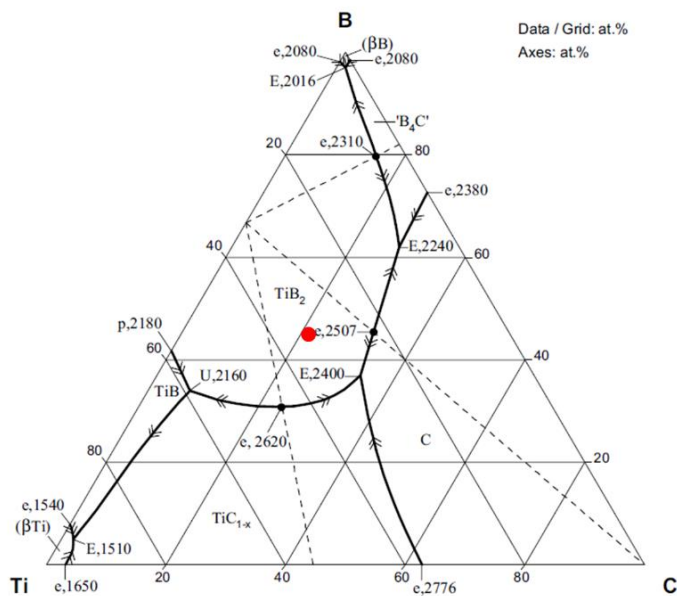


Figure 5.24 – Red dot represents the approximate composition of the spot measured by Figure 5.22, projected on a B-C-Ti ternary phase diagram. Adapted from [105].

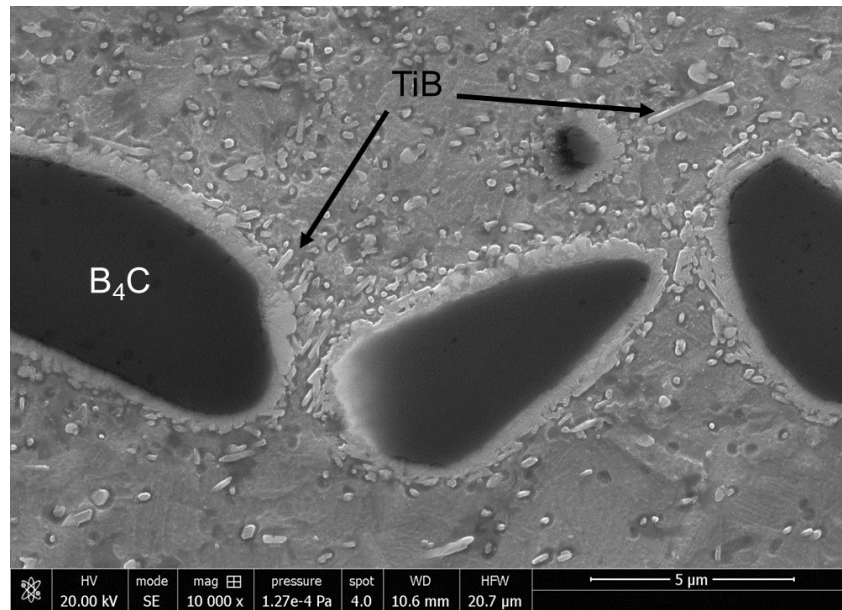


Figure 5.25 - TiB whiskers appearing as a result of degradation of B₄C particles on process runs deposited with rotational speed of 3000 min⁻¹.

While B₄C particles were still present within coatings produced with a rotational speed of 3000 min⁻¹, the reinforcement was barely observed on samples from 6000 min⁻¹ process runs, which led to the conclusion that the dissolution was more severe with increasing rotational speed.

According to [16], no significant increase in process temperature from 3000 to 6000 min⁻¹ occurs, which rules out any possible effects a higher temperature could have on the particle degradation. Instead, this gain in dissolution rate may be attributed to the more intense fracture of particles as the rotational speed rose up, consequence of a higher number of matrix/reinforcement interactions, induced by the higher deformation rate (particle breakage will be addressed in section 5.4.2.2). Instead of the original B₄C particles, trails of a new phase were observed on samples from 6000 min⁻¹ experiments (Figure 5.26 and Figure 5.27).

Qualitative EDS analysis upon those regions indicated the presence of boron and carbon atoms, which could not originate from other source besides the

fully reacted reinforcement particles. As previously mentioned, the newborn phases arising from particles dissolution tend to precipitate in regions such as interfaces and areas with high dislocation density. The fact that those phases appeared not randomly scattered, but instead in well-defined trails is an indicative of the presence of a considerably greater amount of dislocations in such areas comparing to the neighboring regions, which reveals the heterogeneous strain distribution within the deposited material during the process. This feature was also concluded to be responsible for differences in the dynamic recrystallization process on friction-surfaced alloy 625 layers [109]. Moreover, TiB whiskers were more frequent in this case than within samples where particles did not reacted completely (Figure 5.27).

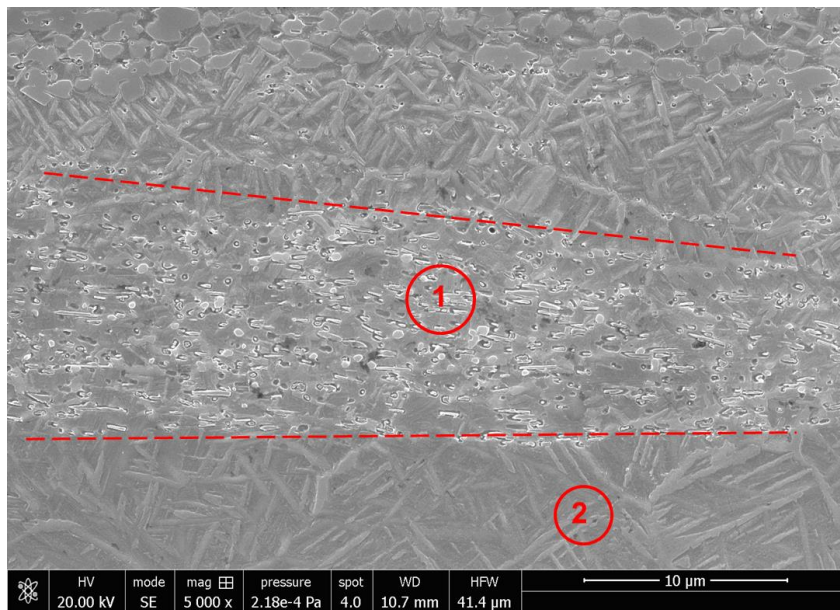


Figure 5.26 - Trail of precipitates delimited by red dashed lines (6000 min^{-1}). EDS analysis performed on the precipitate-rich strip (1) and on a precipitate free surrounding region.

Table 5.2 - Results from EDS measurements on spots (1) and (2), indicated on Figure 5.26.

Element	1		2	
	Weight %	Atomic %	Weight %	Atomic %
B	5.66	17.73	0.00	0.00
C	1.05	2.95	1.69	5.38
N	6.17	14.92	6.41	17.53
Al	5.22	6.55	6.16	8.74
Ti	79.25	56.07	81.72	65.32
V	2.66	1.77	4.01	3.02

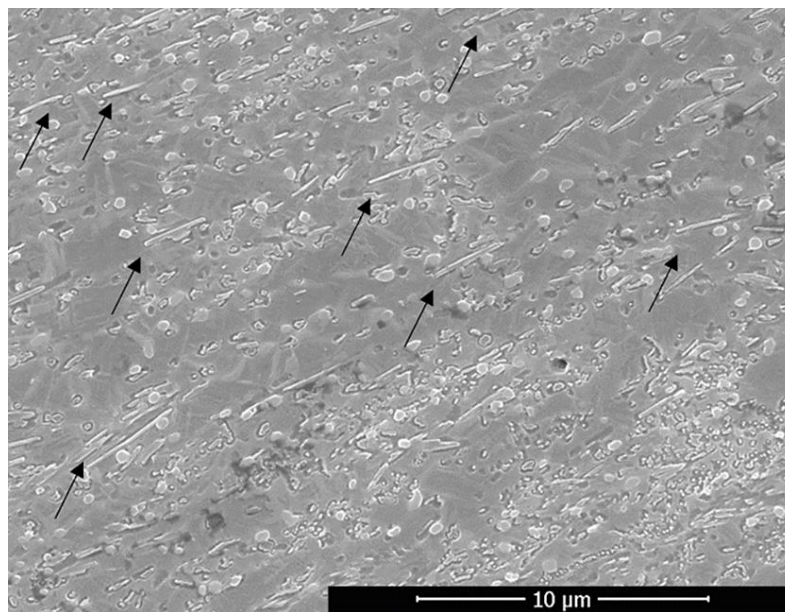


Figure 5.27 - Precipitate-rich region, where TiB whiskers are indicated by black arrows. Rotational speed of 6000 min⁻¹.

5.4.2.1.2. Silicon Carbide

Similarly, particle dissolution could also be observed on samples from process runs with SiC carbide as reinforcement (Figure 5.28). At approx. 1400 K,

the following thermodynamic favorable reaction between SiC particles and Ti matrix takes place [110],:



However, the main difference between SiC and B₄C behavior regarding particle dissolution relies upon the fact that while a rotational speed of 6000 min⁻¹ promoted almost total reaction of the inserted B₄C reinforcement particle, the same effect could not be observed on samples with SiC particles obtained with the same process parameters.

In practical terms, the differences in degradation rate between different reinforcement materials can be analyzed under two different points of view. The first one concerns the ability of some reinforcement materials (SiC in Ti-6Al-4V, for example) to withstand higher rotational speeds during the process, which allows one to produce more homogeneous FS coatings [64] without complete reinforcement degradation.

On the other hand, the severe dissolution of particles (such as B₄C under high rotational speeds in this study) may lead to the emergence of refined hard phases (TiC, TiB and TiB₂ in the present case), which still may improve mechanical properties of the composite. Moreover, the fact that those new-born phases tend to precipitate in high dislocation density areas (result of the complex material flow [79] and thus present all across the coating) may lead to good reinforcement homogeneity along the composite.

This feature stands as an advantage in comparison to the reinforcement distribution patterns obtained solely by the flux of (insoluble) TiC particles during the deposition, which rely heavily upon hole placement on the consumable rod, as demonstrated early.

Another noteworthy point that possibly contribute to the use of unstable particles instead of stable ones is the fact that a batch of large particles (for example, B₄C were 99% < 14 μm acc. to supplier data) can be reduced to sub-micron precipitates deposited within the coating after the process. On the other

hand, a batch of sub-micron stable particles such as TiC is considerably more expensive than the one used here (99% < 4 μm acc. to supplier data), and this certainly would constitute an important obstacle on an eventual industrial application.

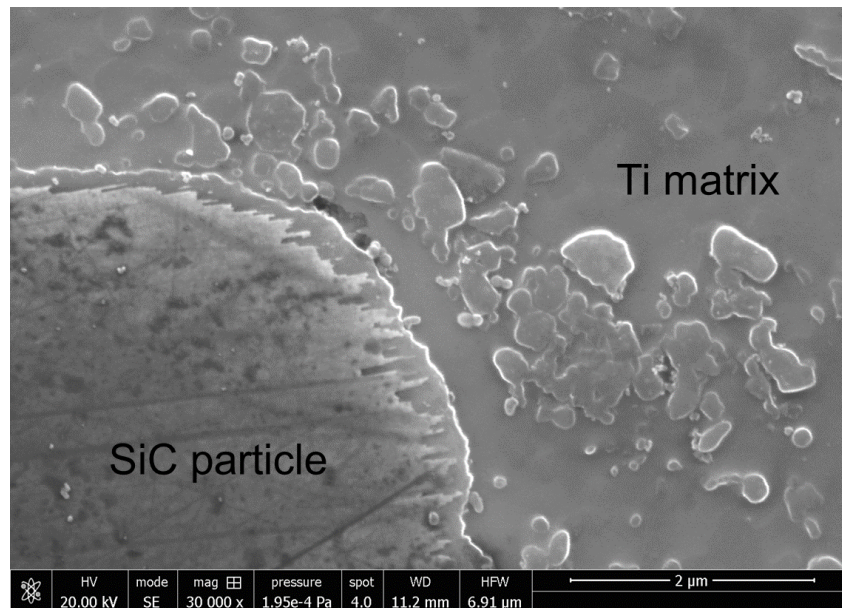


Figure 5.28 - SiC particle partially dissolved. Rotational speed of 6000 min^{-1} .

5.4.2.2. Particle fracture

Due to the high thermodynamic stability of TiC particles, those were selected to have their diameter measured before and after the process (deposited, 6000 min^{-1}) by OM and SEM images. This factors out any dissolution phenomena. Random particles were measured for both situations. The results are displayed in Figure 5.29.

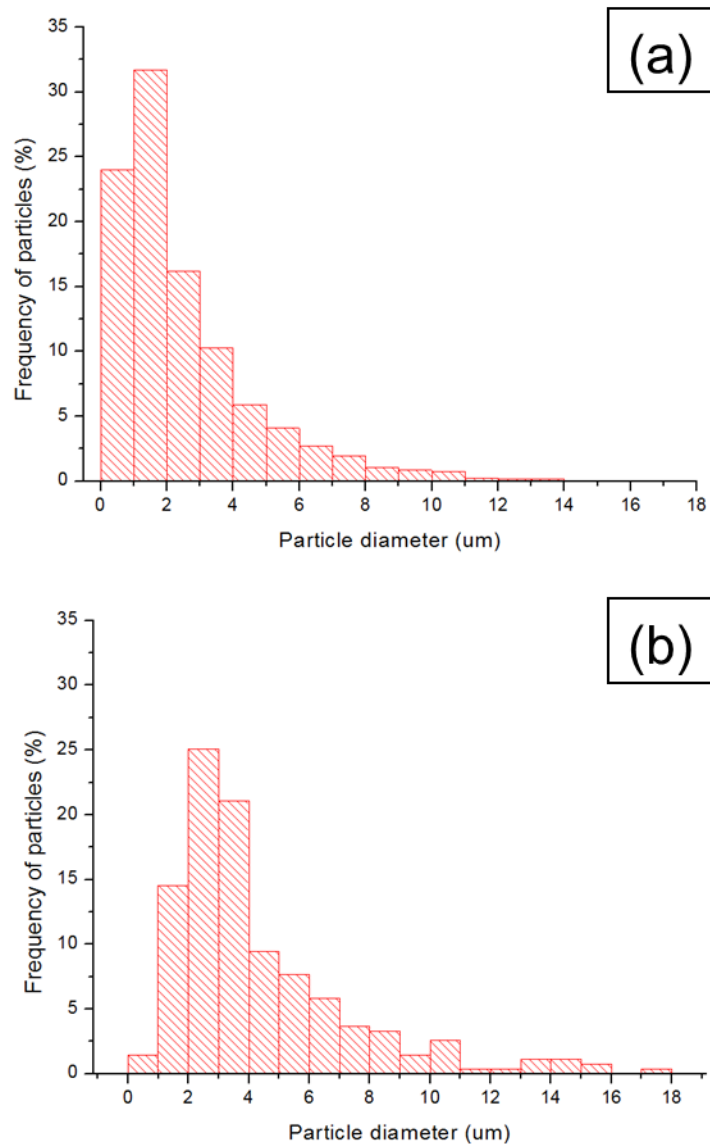


Figure 5.29 - Particle size distribution for deposited TiC particles (a) and TiC particles before the process (b), according to measurements performed on OM and SEM images

There was a meaningful decrease in size of particles after the process, which indicates that particles fractured into smaller parts during the deposition. The main mechanism of reinforcement fracture proposed in the current study consists in particles, located along shear flow paths during the deposition, grating in the direction of the material flow. The metal flowing along those paths transports the resultant debris, leaving fragments trailing the grated particle. An

indication supporting this hypothesis is the shape of large particles located within deposition trails, which is commonly elongated parallel to the trail itself.

According to this explanation, such an elongated shape would be caused by the surrounding material flow along the path, breaking the particle in a very particular direction, and smearing small fractured fragments along a specific direction, see Figure 5.30. The formation of debris off large particles may account for a significant reduction in particle size after the process. In spite of the dissolution phenomenon, the same pattern can be observed in experiments with SiC, see Figure 5.31. In this particular case, it is also possible to observe few large particles (around 10 to 20 μm) elongated in a direction parallel to the particle trails.

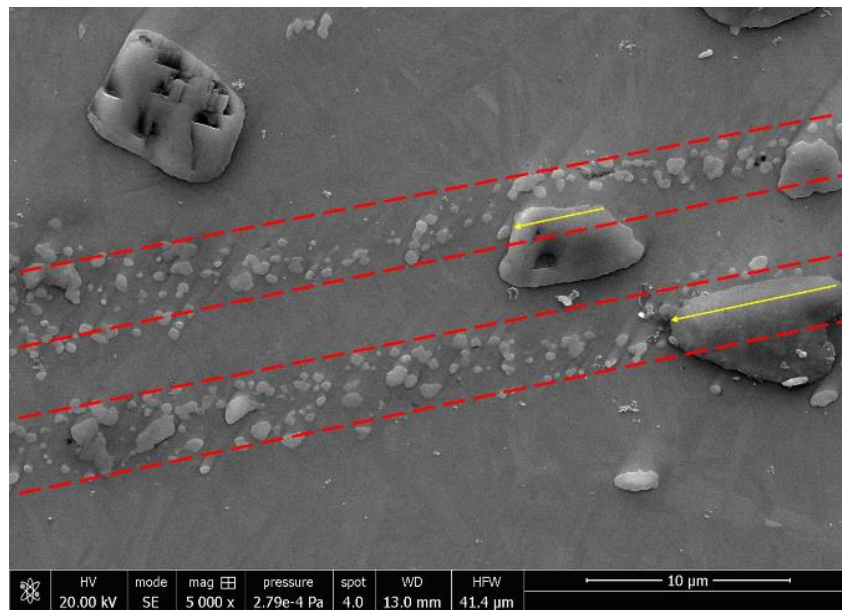


Figure 5.30 – Small TiC particles along shear flow paths (delimited by red dashed lines). Larger particles within those paths elongated in a direction showed by yellow arrows.

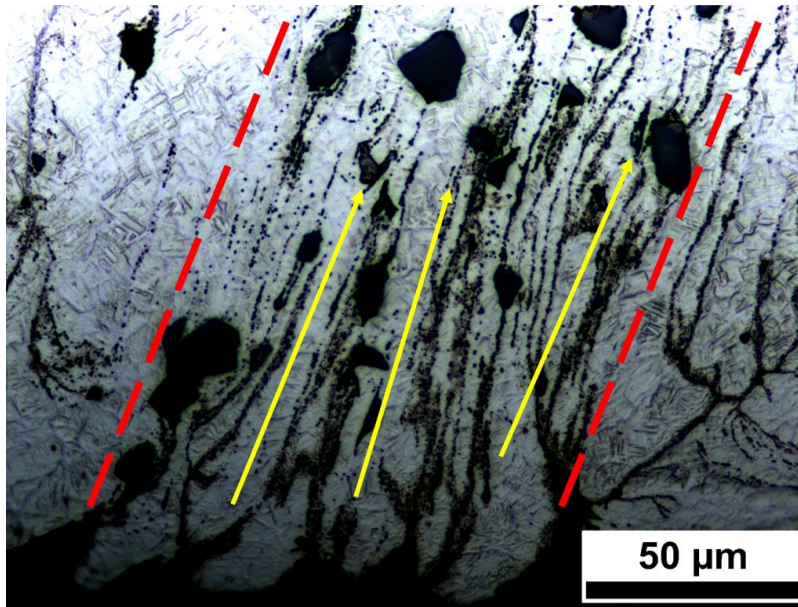


Figure 5.31 – OM image of small SiC particles deposited in parallel to the yellow arrows within a shear flow path delimited by the red dashed lines. No important effects of particle dissolution were observed, as the rotational speed (3000 min^{-1}) was not sufficient to degrade the reinforcement.

In terms of composite reinforcement, the elusive positive effects of a particle size reduction due to breakage on mechanical properties may be non-existent in this case. As discussed in section 5.4.1, the main reason behind the poor performance of coatings on microhardness tests relies upon the fact that particles are not randomly scattered, but instead deposited along trails, distribution which has little effect on grain size reduction during dynamic recrystallization and therefore no noticeable improvement on a number of mechanical properties. Particle debris formed upon breakage are dispersed along the exact same paths where main particles are deposited, which means that neighboring regions will still be mostly reinforcement-free.

A considerably less frequent occurrence happened when particles were densely deposited into a small volume. This usually can be observed when poor particle mixture occurs, which mostly happen (but not only) to holes drilled right at or near to the rod center, as discussed previously. In such situations, the metal matrix may not be able to accommodate all the reinforcement deposited in a

restricted volume, and consequently may crack upon cooling [35,111]. The crack then proceeds to propagate across the material, until it reaches a particle or a group thereof. In this case, the particle(s) may not be able to deflect the crack, causing them to suffer breakage, as evidenced by Figure 5.32.

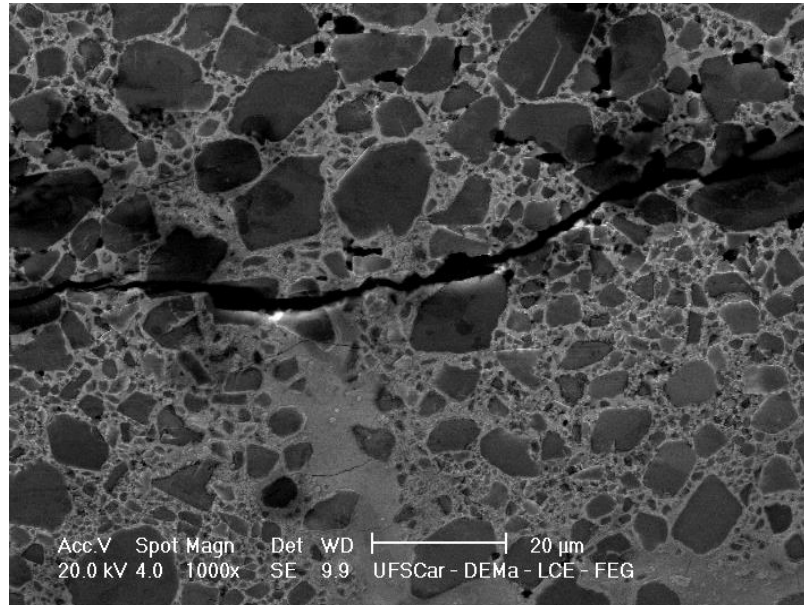


Figure 5.32 - Crack observed on a coating obtained from experiment with SiC particles. The borehole drilled at the rod center in this case contributed to poor mixture of reinforcement. Rotational speed of 6000 min^{-1} .

6. GENERAL DISCUSSION

By adding holes filled of particles on the consumable rod, the FS process is capable of incorporating reinforcement to the Ti-6Al-4V coatings to generate a composite. However, at the current stage it is very clear that the process as presented here has an extensive array of critical problems. Until those problems are overcome, transferring over the process from the laboratory to the industry is not viable (both technically and economically), as there are far better alternatives to improve surface properties currently, with lower cost and waste. Therefore, the studied process at the moment is still not technically feasible.

Although the wear resistance was not analyzed in the present work, it is possible to speculate on the wear behavior of reinforced coatings using the current results as a base. It is true that hardness does not necessarily equal to wear resistance, since there are at least four main wear mechanisms (namely abrasion, adhesion, surface fatigue and tribochemical reaction [112]), which depend upon several factors. However, when it comes to abrasion resistance particularly, the wear rate (or total volume of wear debris) is inversely proportional to the material hardness [15,96]. Since there was no sensible hardness increase upon the addition of particles, one should not expect that the abrasion resistance improved on reinforced samples, in comparison to particle-free coatings.

Another common wear scenario happens when fretting occurs. Fretting wear is a more complex wear mechanism, which takes place between contact surfaces in oscillatory motion at low amplitude (10 to 300 μm [14]), under load [15]. In such cases, Fitseva et al. already demonstrated that, for titanium alloys deposited by FS, fretting wear can be diminished, providing that the grain size was small enough [113]. Grain size, in turn, depends on the rotational speed. A rotational speed of 400 min^{-1} produces fine grains, whereas 6000 min^{-1} (implemented in this work) yields a coarser microstructure [16]. From this point, the reinforced coatings here studied could be viewed under two different perspectives. First, since grain size reduction virtually did not take place upon particle reinforcement, it is reasonable to expect that particles' presence do not

lead to an enhancement on fretting resistance. Second, low rotational speeds reduce heat input and therefore coatings deposited with rotational speeds as low as 400 min^{-1} demand higher axial forces to be completed [64]. The presence of particles on the process zone may make the deposition even more difficult than it already is at high rotational speeds. Either way, the FS process with particles seemingly does not constitute a reliable alternative to improve fretting resistance either.

On the other hand, adhesive wear (or galling) resistance is not necessarily dependent of hardness or grain size *per se* [114]. Among the factors dictating the effectiveness of a given material to contain adhesion wear is the ductility [15]. Processing routes and modifications that decrease that property may potentially increase adhesive wear resistance. The relationship between the addition of particles and ductility was not determined by this work.

For all those reasons, even though still at an early stage, the implement of particles to the FS process of titanium alloys appears to bring along considerably more disadvantages than advantages.

7. CONCLUSIONS

Ti-6Al-4V FS coatings reinforced with carbide particles (TiC, B₄C and SiC) can be produced. However, the process is not reliable due to the following reasons:

- The process is highly sensitive to modifications on the consumable rod. Poorly-chosen hole geometries lead to high axial forces, low deposition efficiency and irregular coatings. Among all nine conditions tested, one hole drilled at 5 mm off the rod center seems to result in the best compromise between coating quality, axial force and efficiency in particle incorporation.
- Regardless of hole geometry, a generally low quantity of the powder inserted into the consumable rod is transferred to the coating. The majority of it is lost either to the immediate surroundings or to the flash. Increasing the number of holes appears to have little effect on the amount of deposited particles, even at expense of an increase in wasted material.
- Deposited particles are not evenly distributed along the coating. Macroscopically, wide particle-free gaps can be observed all over the coatings, regardless of hole geometry. Microscopically, particles are distributed along trails and therefore not randomly dispersed. Thus, they have virtually no positive effect on recrystallized grain size nor on hardness and consequently on a number of related mechanical properties. Moreover, the presence of densely-packed particles may induce pores and matrix cracking.
- Some types of particles may dissolve during the process, depending on the thermodynamics of the reinforcement. New phases normally nucleate either around the particles (incomplete dissolution) or at dislocation-dense areas (complete dissolution). An increase in dissolution can be observed upon rotational speed increase. This is credited to the more intense particle breakage, which increases surface area and reduces dissolution time.
- Equiaxed alpha grains are observed on coatings. They do not depend on particle presence. Shear banding is attributed as the cause to that microstructure.

Although considerably harder than other areas, those regions tend to have voids, which may eventually coalesce to form pores.

8. SUGGESTIONS FOR FUTURE RESEARCH

- Evaluate wear resistance of deposited coatings, especially the adhesive wear mechanism.
- Since particles, pores and de-bonded zones may act as nucleation sites for cracks, it is important to evaluate the performance of reinforced coatings under fatigue as well.
- Further explore the area between 2 mm and 5 mm from the rod center as a region to drill holes. There should be a sweet spot between those marks whereby coatings are able to retain more particles (a “2 mm” characteristic) while showing good coating quality (a “5 mm” one).
- Explore different hole diameters. Spreading the total particle amount over several narrower holes reduces particle clustering, which eases the material flow. This alternative may lead to lower axial forces and consequently higher coating quality overall.
- Apply the same configurations on samples reinforced with instable particles, such as B_4C . After total dissolution, nucleated phases are usually finer and better distributed than particles that do not react (TiC).

9. REFERENCES

- [1] G.S. Cole, A.M. Sherman, Light weight materials for automotive applications, *Mater. Charact.* 35 (1995) 3–9. doi:10.1016/1044-5803(95)00063-1.
- [2] H. ElMaraghy, F. Andersson, A. Hagqvist, E. Sundin, M. Björkman, Design for Manufacturing of Composite Structures for Commercial Aircraft – The Development of a DFM Strategy at SAAB Aerostructures, *Procedia CIRP.* 17 (2014) 362–367. doi:10.1016/j.procir.2014.02.053.
- [3] E.A. Feest, Metal matrix composites for industrial application, *Mater. Des.* 7 (1986) 58–64. doi:10.1016/S0261-3069(86)80002-4.
- [4] K. Creehan, J.P. Schultz, Self-reacting friction stir welding tool with the ability to add filler material, US20120279442 A1, n.d.
- [5] G.M. Reddy, A.S. Rao, K.S. Rao, Friction Stir Surfacing Route: Effective Strategy for the Enhancement of Wear Resistance of Titanium Alloy, *Trans. Indian Inst. Met.* 66 (2013) 231–238. doi:10.1007/s12666-013-0254-x.
- [6] G.J. Fernandez, L.E. Murr, Characterization of tool wear and weld optimization in the friction-stir welding of cast aluminum 359+20% SiC metal-matrix composite, *Mater. Charact.* 52 (2004) 65–75. doi:10.1016/j.matchar.2004.03.004.
- [7] J.C.F. H. J. Liu, Wear characteristics of a WC-Co tool in friction stir welding of AC4AC30 vol% SiCp composite, *Int. J. Mach. Tools Amp Manuf. - INT J MACH TOOL MANUF.* 45 (2005) 1635–1639. doi:10.1016/j.ijmachtools.2004.11.026.
- [8] G.M. Bedfordt, R.P. Sharp, B.J. Wilson, L.G. Elias, Production of friction surfaced components using steel metal matrix composites produced by Osprey process, *Surf. Eng.* 10 (1994) 118–122. doi:10.1179/sur.1994.10.2.118.
- [9] G.M. Reddy, K.S. Rao, T. Mohandas, Friction surfacing: novel technique for metal matrix composite coating on aluminium–silicon alloy, *Surf. Eng.* 25 (2009) 25–30. doi:10.1179/174329408X298238.

- [10] K.S.P. G Madhusudhan Reddy, Friction surfacing of titanium alloy with aluminium metal matrix composite, *Surf. Eng.* 27 (2011) 92–98. doi:10.1179/174329409X451128.
- [11] J. Gandra, P. Vigarinho, D. Pereira, R.M. Miranda, A. Velhinho, P. Vilaça, Wear characterization of functionally graded Al–SiC composite coatings produced by Friction Surfacing, *Mater. Des.* 52 (2013) 373–383. doi:10.1016/j.matdes.2013.05.059.
- [12] G.M. Karthik, G.D.J. Ram, R.S. Kottada, Friction deposition of titanium particle reinforced aluminum matrix composites, *Mater. Sci. Eng. A.* 653 (2016) 71–83. doi:10.1016/j.msea.2015.12.005.
- [13] K. Miyoshi, *Solid Lubrication Fundamentals and Applications*, CRC Press, 2001.
- [14] K.G. Budinski, Tribological properties of titanium alloys, *Wear.* 151 (1991) 203–217. doi:10.1016/0043-1648(91)90249-T.
- [15] S. Loredana, *Surface Engineering Techniques and Applications: Research Advancements: Research Advancements*, IGI Global, 2014.
- [16] V. Fitseva, S. Hanke, J.F. dos Santos, P. Stemmer, B. Gleising, The role of process temperature and rotational speed in the microstructure evolution of Ti-6Al-4V friction surfacing coatings, *Mater. Des.* 110 (2016) 112–123. doi:10.1016/j.matdes.2016.07.132.
- [17] G. Lütjering, J.C. Williams, *Titanium*, 2nd ed., Springer, 2007.
- [18] J. Dai, J. Zhu, C. Chen, F. Weng, High temperature oxidation behavior and research status of modifications on improving high temperature oxidation resistance of titanium alloys and titanium aluminides: A review, *J. Alloys Compd.* 685 (2016) 784–798. doi:10.1016/j.jallcom.2016.06.212.
- [19] J. Unnam, R.N. Shenoy, R.K. Clark, Oxidation of commercial purity titanium, *Oxid. Met.* 26 (1986) 231–252. doi:10.1007/BF00659186.
- [20] R. Gaddam, B. Sefer, R. Pederson, M.-L. Antti, Oxidation and alpha-case formation in Ti–6Al–2Sn–4Zr–2Mo alloy, *Mater. Charact.* 99 (2015) 166–174. doi:10.1016/j.matchar.2014.11.023.
- [21] J. Sieniawski, W. Ziąja, K. Kubiak, M. Motyk, Microstructure and Mechanical Properties of High Strength Two-Phase Titanium Alloys, in: J.

- Sieniawski (Ed.), Titan. Alloys - Adv. Prop. Control, InTech, 2013. <http://www.intechopen.com/books/titanium-alloys-advances-in-properties-control/microstructure-and-mechanical-properties-of-high-strength-two-phase-titanium-alloys> (accessed August 8, 2016).
- [22] J.I. Qazi, O.N. Senkov, J. Rahim, F.H. (Sam) Froes, Kinetics of martensite decomposition in Ti–6Al–4V–xH alloys, *Mater. Sci. Eng. A.* 359 (2003) 137–149. doi:10.1016/S0921-5093(03)00350-2.
- [23] R.E. Smelser, J.L. Swedlow, A continuum analysis of fracture in Widmanstätten α plus β colonies, *Mater. Sci. Eng.* 46 (1980) 175–190. doi:10.1016/0025-5416(80)90174-3.
- [24] J.. Peters, R.. Ritchie, Foreign-object damage and high-cycle fatigue of Ti–6Al–4V, *Mater. Sci. Eng. A.* 319–321 (2001) 597–601. doi:10.1016/S0921-5093(01)00982-0.
- [25] Titanium: Past, Present, and Future □: Report, National Academies, 1983.
- [26] M.-S. Yeh, J.-H. Huang, Hydrogen-induced subcritical crack growth in Ti–6Al–4V alloy, *Mater. Sci. Eng. A.* 242 (1998) 96–107. doi:10.1016/S0921-5093(97)00506-6.
- [27] S. Abkowitz, Titanium in industry: technology of structural titanium, Van Nostrand, 1955.
- [28] M. Niinomi, Recent titanium R&D for biomedical applications in japan, *JOM.* 51 (1999) 32–34. doi:10.1007/s11837-999-0091-x.
- [29] S.T. Oyama, *The Chemistry of Transition Metal Carbides and Nitrides*, Springer Science & Business Media, 2012.
- [30] H.O. Pierson, 3 - Interstitial Carbides, Structure and Composition, in: *Handb. Refract. Carbides Nitrides*, William Andrew Publishing, Westwood, NJ, 1996: pp. 17–54. doi:10.1016/B978-081551392-6.50004-0.
- [31] H.O. Pierson, 4 - Carbides of Group IV: Titanium, Zirconium, and Hafnium Carbides, in: *Handb. Refract. Carbides Nitrides*, William Andrew Publishing, Westwood, NJ, 1996: pp. 55–80. doi:10.1016/B978-081551392-6.50005-2.

- [32] H.O. Pierson, 7 - Covalent Carbides: Structure and Composition, in: *Handb. Refract. Carbides Nitrides*, William Andrew Publishing, Westwood, NJ, 1996: pp. 118–136. doi:10.1016/B978-081551392-6.50008-8.
- [33] H.O. Pierson, 8 - Characteristics and Properties of Silicon Carbide and Boron Carbide, in: *Handb. Refract. Carbides Nitrides*, William Andrew Publishing, Westwood, NJ, 1996: pp. 137–155. doi:10.1016/B978-081551392-6.50009-X.
- [34] P. Pirouz, M. Zhang, J.-L. Demenet, H.M. Hobgood, Transition from brittleness to ductility in SiC, *J. Phys. Condens. Matter.* 14 (2002) 12929. doi:10.1088/0953-8984/14/48/335.
- [35] Z.Y. Ma, J. Bi, Y.X. Lu, M. Luo, Y.X. Gao, Quench strengthening mechanism of AL-SiC composites, *Scr. Metall. Mater.* 29 (1993) 225–229. doi:10.1016/0956-716X(93)90313-H.
- [36] W.S. Miller, F.J. Humphreys, Strengthening mechanisms in particulate metal matrix composites, *Scr. Metall. Mater.* 25 (1991) p 33-38.
- [37] J. Gil Sevillano, I. Ocaña Arizcorreta, L.P. Kubin, Intrinsic size effects in plasticity by dislocation glide, *Mater. Sci. Eng. A.* 309–310 (2001) 393–405. doi:10.1016/S0921-5093(00)01733-0.
- [38] M.E. Kassner, M.-T. Pérez-Prado, Chapter 8 - Creep Behavior of Particle-Strengthened Alloys, in: *Fundam. Creep Met. Alloys*, Elsevier Science Ltd, Oxford, 2004: pp. 151–169. <http://www.sciencedirect.com/science/article/pii/B9780080436371500090> (accessed July 21, 2016).
- [39] E. Arzt, Size effects in materials due to microstructural and dimensional constraints: a comparative review, *Acta Mater.* 46 (1998) 5611–5626. doi:10.1016/S1359-6454(98)00231-6.
- [40] E. Orowan, Discussion on Internal Stresses, in: *Symp Intern. Stress. Met. Alloys*, The Institute of Metals, London, 1948: pp. 451–453.
- [41] T. Torma, E. Kovács-Csetényi, T. Turmezey, T. Ungár, I. Kovács, Hardening mechanisms in Al-Sc alloys, *J. Mater. Sci.* 24 (n.d.) 3924–3927. doi:10.1007/BF01168955.

- [42] N. Hansen, Hall–Petch relation and boundary strengthening, *Scr. Mater.* 51 (2004) 801–806. doi:10.1016/j.scriptamat.2004.06.002.
- [43] J.D. Robson, D.T. Henry, B. Davis, Particle effects on recrystallization in magnesium–manganese alloys: Particle-stimulated nucleation, *Acta Mater.* 57 (2009) 2739–2747. doi:10.1016/j.actamat.2009.02.032.
- [44] L.P. Troeger, E.A. Starke Jr, Particle-stimulated nucleation of recrystallization for grain-size control and superplasticity in an Al–Mg–Si–Cu alloy, *Mater. Sci. Eng. A.* 293 (2000) 19–29. doi:10.1016/S0921-5093(00)01235-1.
- [45] R.D. Doherty, D.A. Hughes, F.J. Humphreys, J.J. Jonas, D.J. Jensen, M.E. Kassner, W.E. King, T.R. McNelley, H.J. McQueen, A.D. Rollett, Current issues in recrystallization: a review, *Mater. Sci. Eng. A.* 238 (1997) 219–274. doi:10.1016/S0921-5093(97)00424-3.
- [46] K. Chang, J. Kwon, C.-K. Rhee, Role of second-phase particle morphology on 3D grain growth: A phase-field approach, *Comput. Mater. Sci.* 124 (2016) 438–443. doi:10.1016/j.commatsci.2016.08.019.
- [47] K. Chang, W. Feng, L.-Q. Chen, Effect of second-phase particle morphology on grain growth kinetics, *Acta Mater.* 57 (2009) 5229–5236. doi:10.1016/j.actamat.2009.07.025.
- [48] T. Nishizawa, I. Ohnuma, K. Ishida, Examination of the Zener Relationship between Grain Size and Particle Dispersion, *Mater. Trans. JIM.* 38 (1997) 950–956. doi:10.2320/matertrans1989.38.950.
- [49] R.S. Mishra, M.W. Mahoney, *Friction Stir Welding and Processing*, ASM International, 2007.
- [50] J. Gandra, H. Krohn, R.M. Miranda, P. Vilaça, L. Quintino, J.F. dos Santos, Friction surfacing—A review, *J. Mater. Process. Technol.* 214 (2014) 1062–1093. doi:10.1016/j.jmatprotec.2013.12.008.
- [51] Y. Chen, J. Chen, B.S. Amirkhiz, M.J. Worswick, A.P. Gerlich, Microstructures and properties of Mg alloy/DP600 steel dissimilar refill friction stir spot welds, *Sci. Technol. Weld. Join.* 20 (2015) 494–501. doi:10.1179/1362171815Y.0000000033.

- [52] A.R. Neelands, H. Klopstock, An improved method of joining or welding metals, 572789–A, 1941. <http://www.directorypatent.com/GB/572789-a.html>.
- [53] J. Akram, R. Puli, P.R. Kalvala, M. Misra, A novel weld transition joint by friction surfacing, *Manuf. Lett.* 2 (2014) 104–107. doi:10.1016/j.mfglet.2014.07.004.
- [54] J. Gandra, D. Pereira, R.M. Miranda, P. Vilaça, Influence of Process Parameters in the Friction Surfacing of AA 6082-T6 over AA 2024-T3, *Procedia CIRP.* 7 (2013) 341–346. doi:10.1016/j.procir.2013.05.058.
- [55] R. M., J. Gandra, P. Vila, Surface Modification by Friction Based Processes, in: M. Aliofkhazraei (Ed.), *Mod. Surf. Eng. Treat.*, InTech, 2013. <http://www.intechopen.com/books/modern-surface-engineering-treatments/surface-modification-by-friction-based-processes> (accessed August 8, 2016).
- [56] U. Suhuddin, S. Mironov, H. Krohn, M. Beyer, J.F.D. Santos, Microstructural Evolution During Friction Surfacing of Dissimilar Aluminum Alloys, *Metall. Mater. Trans. A.* 43 (2012) 5224–5231. doi:10.1007/s11661-012-1345-8.
- [57] H. Krohn, S. Hanke, M. Beyer, J.F. dos Santos, Influence of external cooling configuration on friction surfacing of AA6082 T6 over AA2024 T351, *Manuf. Lett.* 5 (2015) 17–20. doi:10.1016/j.mfglet.2015.04.004.
- [58] S. Hanke, M. Beyer, J.F. dos Santos, A. Fischer, Friction surfacing of a cold work tool steel—Microstructure and sliding wear behavior, *Wear.* 308 (2013) 180–185. doi:10.1016/j.wear.2013.06.017.
- [59] D. Pereira, J. Gandra, J. Pamies-Teixeira, R.M. Miranda, P. Vilaça, Wear behaviour of steel coatings produced by friction surfacing, *J. Mater. Process. Technol.* 214 (2014) 2858–2868. doi:10.1016/j.jmatprotec.2014.06.003.
- [60] R. Sekharbabu, H.K. Rafi, K.P. Rao, Characterization of D2 tool steel friction surfaced coatings over low carbon steel, *Mater. Des.* 50 (2013) 543–550. doi:10.1016/j.matdes.2013.03.042.

- [61] S. Hanke, M. Beyer, A. Silvonen, J.F. dos Santos, A. Fischer, Cavitation erosion of Cr60Ni40 coatings generated by friction surfacing, *Wear*. 301 (2013) 415–423. doi:10.1016/j.wear.2012.11.016.
- [62] K. Prasad Rao, A. Veera Sreenu, H. Khalid Rafi, M.N. Libin, K. Balasubramaniam, Tool steel and copper coatings by friction surfacing – A thermography study, *J. Mater. Process. Technol.* 212 (2012) 402–407. doi:10.1016/j.jmatprotec.2011.09.023.
- [63] K.P. Rao, R. Damodaram, H.K. Rafi, G.D.J. Ram, G.M. Reddy, R. Nagalakshmi, Friction surfaced Stellite6 coatings, *Mater. Charact.* 70 (2012) 111–116. doi:10.1016/j.matchar.2012.05.008.
- [64] V. Fitseva, H. Krohn, S. Hanke, J.F. dos Santos, Friction surfacing of Ti–6Al–4V: Process characteristics and deposition behaviour at various rotational speeds, *Surf. Coat. Technol.* 278 (2015) 56–63. doi:10.1016/j.surfcoat.2015.07.039.
- [65] V. Fitseva, S. Hanke, J.F. dos Santos, Influence of rotational speed on process characteristics, material flow and microstructure evolution in Friction Surfacing of Ti-6Al-4V, (2016). <http://www.smt30.org/>.
- [66] G.M. Bedford, V.I. Vitanov, I.I. Voutchkov, On the thermo-mechanical events during friction surfacing of high speed steels, *Surf. Coat. Technol.* 141 (2001) 34–39. doi:10.1016/S0257-8972(01)01129-X.
- [67] A.A. Shirzadi, H. Assadi, E.R. Wallach, Interface evolution and bond strength when diffusion bonding materials with stable oxide films, *Surf. Interface Anal.* 31 (2001) 609–618. doi:10.1002/sia.1088.
- [68] K.P. Rao, R. Damodaram, H.K. Rafi, G.D.J. Ram, G.M. Reddy, R. Nagalakshmi, Friction surfaced Stellite6 coatings, *Mater. Charact.* 70 (2012) 111–116. doi:10.1016/j.matchar.2012.05.008.
- [69] R. Puli, G.D. Janaki Ram, Corrosion performance of AISI 316L friction surfaced coatings, *Corros. Sci.* 62 (2012) 95–103. doi:10.1016/j.corsci.2012.04.050.
- [70] I. Voutchkov, B. Jaworski, V.I. Vitanov, G.M. Bedford, An integrated approach to friction surfacing process optimisation, *Surf. Coat. Technol.* 141 (2001) 26–33. doi:10.1016/S0257-8972(01)01127-6.

- [71] J.Q. Li, T. Shinoda, Underwater friction surfacing, *Surf. Eng.* 16 (2000) 31–35. doi:10.1179/026708400322911483.
- [72] Friction Surfacing for Multi-Sectorial Applications » Nordseetaucher GmbH, (n.d.). <http://www.nordseetaucher.de/research-and-development/hyperbaric-welding/friction-surfacing-for-multi-sectorial-applications/> (accessed August 4, 2016).
- [73] Y. YAMASHITA, K. FUJITA, Newly Developed Repairs on Welded Area of LWR Stainless Steel by Friction Surfacing, *J. Nucl. Sci. Technol.* 38 (2001) 896–900. doi:10.1080/18811248.2001.9715112.
- [74] R.W. Doughty, D.J. Shaw, D.E. Gibson, Friction stir surfacing process and device for treating rails, WO2009030960 A1, 2009. <http://www.google.ch/patents/WO2009030960A1> (accessed August 4, 2016).
- [75] K.H. Stern, *Metallurgical and Ceramic Protective Coatings*, Springer Science & Business Media, 2012.
- [76] TMC 45 - Frictec, (n.d.). <http://www.frictec.com/en/tmc45> (accessed August 4, 2016).
- [77] B. Jaworski, I.I. Voutchkov, V.I. Vitanov, V. Hughes, Modelling of the Friction Surfacing Process for Turbine Blade Reclamation, (2000) 307–312. doi:10.1007/978-1-4471-0777-4_48.
- [78] S.F. Miller, S.G. Arul, G.H. Kruger, T.-Y. Pan, A.J. Shih, Effect of Localized Metal Matrix Composite Formation on Spot Friction Welding Joint Strength, *J. Eng. Mater. Technol.* 133 (2011) 031009–031009. doi:10.1115/1.4004389.
- [79] H.K. Rafi, G. Phanikumar, K.P. Rao, Material Flow Visualization during Friction Surfacing, *Metall. Mater. Trans. A.* 42 (2011) 937–939. doi:10.1007/s11661-011-0614-2.
- [80] K. Fukakusa, On Characteristics of Real Rotational Contact Plane, *Q. J. Jpn. Weld. Soc.* 14 (1996) 33–38. doi:10.2207/qjjws.14.33.
- [81] T. Ahmed, H.J. Rack, Phase transformations during cooling in $\alpha+\beta$ titanium alloys, *Mater. Sci. Eng. A.* 243 (1998) 206–211. doi:10.1016/S0921-5093(97)00802-2.

- [82] G. Lütjering, J.C. Williams, A. Gysler, Microstructure and mechanical properties of titanium alloys, in: *Microstruct. Prop. Mater.*, WORLD SCIENTIFIC, 2000: pp. 1–77. http://www.worldscientific.com/doi/abs/10.1142/9789812793959_0001 (accessed January 5, 2017).
- [83] M.A. Meyers, H.-R. Pak, Observation of an adiabatic shear band in titanium by high-voltage transmission electron microscopy, *Acta Metall.* 34 (1986) 2493–2499. doi:10.1016/0001-6160(86)90152-5.
- [84] S.P. Timothy, I.M. Hutchings, The structure of adiabatic shear bands in a titanium alloy, *Acta Metall.* 33 (1985) 667–676. doi:10.1016/0001-6160(85)90030-6.
- [85] J.L. Sun, P.W. Trimby, F.K. Yan, X.Z. Liao, N.R. Tao, J.T. Wang, Shear banding in commercial pure titanium deformed by dynamic compression, *Acta Mater.* 79 (2014) 47–58. doi:10.1016/j.actamat.2014.07.011.
- [86] Z.X. Zhang, S.J. Qu, A.H. Feng, J. Shen, D.L. Chen, Hot deformation behavior of Ti-6Al-4V alloy: Effect of initial microstructure, *J. Alloys Compd.* 718 (2017) 170–181. doi:10.1016/j.jallcom.2017.05.097.
- [87] T. Seshacharyulu, S.C. Medeiros, W.G. Frazier, Y.V.R.K. Prasad, Hot working of commercial Ti-6Al-4V with an equiaxed α - β microstructure: materials modeling considerations, *Mater. Sci. Eng. A.* 284 (2000) 184–194. doi:10.1016/S0921-5093(00)00741-3.
- [88] A. Dehghan-Manshadi, R.J. Dippenaar, Strain-induced phase transformation during thermo-mechanical processing of titanium alloys, *Mater. Sci. Eng. A.* 552 (2012) 451–456. doi:10.1016/j.msea.2012.05.069.
- [89] A.M. Jorge Junior, L.H. Guedes, O. Balancin, Ultra Grain Refinement During the Simulated Thermomechanical-processing of Low Carbon Steel, *J. Mater. Res. Technol.* 1 (2012) 141–147. doi:10.1016/S2238-7854(12)70025-X.
- [90] Q. Xue, M.A. Meyers, V.F. Nesterenko, Self-organization of shear bands in titanium and Ti-6Al-4V alloy, *Acta Mater.* 50 (2002) 575–596. doi:10.1016/S1359-6454(01)00356-1.

- [91] Y.-L. Shen, N. Chawla, On the correlation between hardness and tensile strength in particle reinforced metal matrix composites, *Mater. Sci. Eng. A.* 297 (2001) 44–47. doi:10.1016/S0921-5093(00)01256-9.
- [92] J. Datsko, L. Hartwig, B. McClory, On the tensile strength and hardness relation for metals, *J. Mater. Eng. Perform.* 10 (2001) 718–722. doi:10.1361/105994901770344601.
- [93] S.C. Krishna, N.K. Gangwar, A.K. Jha, B. Pant, On the Prediction of Strength from Hardness for Copper Alloys, *J. Mater.* 2013 (2013) 1–6. doi:10.1155/2013/352578.
- [94] K.-S. Lee, J.-H. Song, Estimation methods for strain-life fatigue properties from hardness, *Int. J. Fatigue.* 28 (2006) 386–400. doi:10.1016/j.ijfatigue.2005.07.037.
- [95] A. Casagrande, G.P. Cammarota, L. Micele, Relationship between fatigue limit and Vickers hardness in steels, *Mater. Sci. Eng. A.* 528 (2011) 3468–3473. doi:10.1016/j.msea.2011.01.040.
- [96] J.F. Archard, Contact and Rubbing of Flat Surfaces, *J. Appl. Phys.* 24 (1953) 981–988. doi:10.1063/1.1721448.
- [97] H. Uzun, Friction stir welding of SiC particulate reinforced AA2124 aluminium alloy matrix composite, *Mater. Des.* 28 (2007) 1440–1446. doi:10.1016/j.matdes.2006.03.023.
- [98] H. Nami, H. Adgi, M. Sharifitabar, H. Shamabadi, Microstructure and mechanical properties of friction stir welded Al/Mg₂Si metal matrix cast composite, *Mater. Des.* 32 (2011) 976–983. doi:10.1016/j.matdes.2010.07.008.
- [99] M.-N. Avettand-Fènoël, A. Simar, A review about Friction Stir Welding of metal matrix composites, *Mater. Charact.* 120 (2016) 1–17. doi:10.1016/j.matchar.2016.07.010.
- [100] R. Abbaschian, R. Reed-Hill, *Physical Metallurgy Principles*, Cengage Learning, 2008.
- [101] R. Bullough, L.C. Davis, The residual deformation fields in particle reinforced metal—matrix composites, *Acta Metall. Mater.* 43 (1995) 2737–2742. doi:10.1016/0956-7151(94)00456-R.

- [102] G.B. Brook, *Smithells Light Metals Handbook*, Butterworth-Heinemann, 1998.
- [103] E. Ustundag, G. Fischman, eds., *23rd Annual Conference on Composites, Advanced Ceramics, Materials, and Structures: B: Ceramic Engineering and Science Proceedings*, Volume 20 Issue 4, John Wiley & Sons, Inc., Hoboken, NJ, USA, 1999. doi:10.1002/9780470294574.
- [104] H. Wang, W. Wu, S. Sun, X. Bian, G. Tu, Characterization of the structure of TiB₂/TiC nanocomposite powders fabricated by high-energy ball milling, *Ceram. Int.* 37 (2011) 2689–2693. doi:10.1016/j.ceramint.2011.04.014.
- [105] Materials Science International Team MSIT®, B-C-Ti (Boron - Carbon - Titanium), in: G. Effenberg, S. Ilyenko (Eds.), *Light Met. Syst. Part 4*, Springer-Verlag, Berlin/Heidelberg, 2006: pp. 1–24. doi:10.1007/11008514_6.
- [106] J. Du, A.P. Sanders, V. Jindal, K.S.R. Chandran, Rapid in situ formation and densification of titanium boride (TiB) nano-ceramic via transient liquid phase in electric field activated sintering, *Scr. Mater.* 123 (2016) 95–99. doi:10.1016/j.scriptamat.2016.06.010.
- [107] M. Selvakumar, P. Chandrasekar, M. Mohanraj, B. Ravisankar, J.N. Balaraju, Role of powder metallurgical processing and TiB reinforcement on mechanical response of Ti–TiB composites, *Mater. Lett.* 144 (2015) 58–61. doi:10.1016/j.matlet.2014.12.126.
- [108] K.B. Panda, K.S.R. Chandran, Titanium-titanium boride (Ti-TiB) functionally graded materials through reaction sintering: Synthesis, microstructure, and properties, *Metall. Mater. Trans. A.* 34 (2003) 1993–2003. doi:10.1007/s11661-003-0164-3.
- [109] S. Hanke, I. Sena, R.S. Coelho, J.F. dos Santos, Microstructural features of dynamic recrystallization in alloy 625 friction surfacing coatings, *Mater. Manuf. Process.* (2017). <http://www.tandfonline.com/doi/abs/10.1080/10426914.2017.1291947> (accessed July 20, 2017).
- [110] I. Gotman, E.Y. Gutmanas, P. Mogilevsky, Interaction between SiC and Ti powder, *J. Mater. Res.* 8 (1993) 2725–2733. doi:10.1557/JMR.1993.2725.

- [111] J. Wang, L. Li, W. Tao, Crack initiation and propagation behavior of WC particles reinforced Fe-based metal matrix composite produced by laser melting deposition, *Opt. Laser Technol.* 82 (2016) 170–182. doi:10.1016/j.optlastec.2016.03.008.
- [112] K.-H.Z. Gahr, ed., Chapter 5 Grooving Wear, in: *Tribol. Ser.*, Elsevier, 1987: pp. 132–350. doi:10.1016/S0167-8922(08)70723-5.
- [113] V. Fitseva, Friction surfacing of titanium grade 1 and Ti-6Al-4V, Thesis, 2017. doi:10.15480/882.1338.
- [114] M. Long, H.J. Rack, Friction and surface behavior of selected titanium alloys during reciprocating-sliding motion, *Wear.* 249 (2001) 157–167. doi:10.1016/S0043-1648(01)00517-8.